

MASTER THESIS

Resilience of electricity grids against transmission line overloads under renewable power injection

A thesis submitted in fulfillment of the requirements for the degree of Master of Science in Physics in the Research Group Maaß
Department of Physics
University of Osnabrück

Author: Christoph Schiel
First examiner: Prof. Dr. P. Maaß
Second examiner: Dr. P. Lind
Submission date: 31.01.2018

Abstract

An increasing proportion of renewable energy sources in power grids leads to the question whether the fluctuations of the two main sources, wind and solar radiation, impact the grids stability. Here we present a method to determine the probability of a single transmission line overload under a fluctuating power injection. This method is based on the linearized power flow equations and a quasi-static response from the grid, and was utilized to estimate the resilience of the *IEEE Reliability Test System 1996* under the replacement of conventional generators by wind farms and the mutual influence of wind power at different nodes. Our research finds that the overload probability depends strongly on the location of the replaced generator and the spatial correlation between pairs of wind farms. Furthermore, we find that it is possible for two wind farms to increase the line power threshold for one node through an increased power injection at the other node. This favorable interaction is connected to the topological distance of the corresponding line from the shortest path between the wind farms.

Zusammenfassung

Ein erhöhter Anteil von erneuerbaren Energiequellen im Stromnetz führt zu der Frage, ob die Fluktuationen der beiden größten Quellen, Wind und Photovoltaik, einen Einfluss auf die Netzstabilität haben. Es wird eine Methode zur Bestimmung der Wahrscheinlichkeit einer überladenen Übertragungsleitung unter Einspeisung von fluktuierender Leistung präsentiert. Diese Methode basiert auf den linearen Lastflussgleichungen und einer quasi-statischen Reaktion des Netzes. Mithilfe dieser Methode wurde die Widerstandsfähigkeit des *IEEE Reliability Test System 1996* gegen Leitungsüberlastungen und der gegenseitige Einfluss von Windleistung an unterschiedlichen Knoten untersucht. Hierfür werden herkömmliche Generatoren durch Windparks ersetzt. Es ergibt sich, dass die Überlastwahrscheinlichkeit stark von dem Standort des ersetzten Generators und den räumlichen Korrelation zwischen Paaren von Windparks abhängt. Des Weiteren beobachten wir ein interessantes Verhalten für zwei Windparks fest: Der kritische Leistungsgrenzwert eines Knoten zu erhöhen, indem der andere Knoten mehr Leistung einspeist. Wir beobachten, dass dieses vorteilhafte Verhalten mit der topologischen Distanz der zugehörigen Leitung von dem kürzesten Pfad zwischen den beiden Windparks abhängt.

Contents

1	Introduction	3
2	Modeling of power grids	5
2.1	Information about todays power grids	5
2.2	Network representation	8
2.2.1	Network model	9
2.2.2	Bus and transmission line model	10
2.2.3	Graph theory	11
2.3	Power flow analysis	13
2.3.1	Power flow equations	13
2.3.2	Power flow study	17
2.4	Available grid data and toolboxes	19
3	Integration of renewable energy sources	21
3.1	Overview of the renewable energy source wind	21
3.2	Modeling renewable sources in the power grid	27
3.2.1	Fluctuating sources in the linear power flow	27
3.2.2	Statistics of line overload probabilities	28
3.3	IEEE test grid resilience against wind power injection	30
3.3.1	Embedding of a single wind farm	31
3.3.2	Embedding of two wind farms	32
3.4	Outlook for the German power grid	38
4	Conclusion	41
A	Supplementary material	43
A.1	Example of an resistive network calculation	43
A.2	Example calculation of the linear power flow equations	45
A.3	Polygon example calculation	46
A.4	Change of variable - Weibull	48
A.5	Numerical method of solving the double integral and optimization	49
A.6	IEEE RTS-96 data tables	53
A.7	Overload probability correlation to topology (unweighted)	54
A.8	QGis and GraphViz for illustrating grids	55
B	Polygons of the IEEE test grid	57

Chapter 1

Introduction

The electrical grid, or power grid, is one of the largest machines ever constructed [1]; the grid is constantly being developed and used to deliver electricity to our everyday lives. Electrical grids consist of generators that produce electrical power and transmission lines that transport the power to consumers while minimizing losses and keeping the grid in a stable state. However, even with today's technology and high security standards failures still occur. On 4 November 2006 the operators of the German power grid performed a planned routine disconnection of an ultra-high voltage transmission line in north west Germany. Thirty minutes after the scheduled line was taken off the grid, the operators initiated countermeasures that exceeded the power threshold for another transmission line. Twenty-eight seconds later, the countermeasures failed and multiple overloaded lines were shut down, which split the European grid into three parts and caused a major blackout for more than 15 million clients [2].

This blackout reflects the impact of a single line outage on the efficiency and reliability of the power grid. However, the current system dynamic will change with a higher proportion of fluctuating power sources, such as wind and solar radiation, and it will be increasingly difficult to guarantee the stability of the grid [3]. The currently implemented control mechanisms maintain the balance between power production and demand by keeping the frequency and voltage stable [4]. With the fluctuating power production from wind and solar power, this control mechanism must be checked. Furthermore, the time scales of the renewable power fluctuations are much smaller than the previous change in demand [5, 6].

One solution would be to avoid the injection of the fluctuating power and store it beforehand. However, storage solutions on this scale are currently limited and can be expensive. For example, the main source of energy storage for power grids are dams, which are unavailable in the mostly flat region of northern Germany where wind power production exceeds demands. The direct injection of the renewable powers to the grid is accompanied by the need for compensation through conventional generators. In the year 2017 the German grid operator *TenneT* spent nearly 1 billion euros on emergency interventions caused by fluctuations of renewable sources [7]. Therefore, optimizing the embedding of renewable energy in respect to the necessary conventional generators is an objective of interest, for which a model of the power grid is required.

To tackle problem of modeling power grids, a combination of methods developed in the fields of nonlinear dynamics, network theory and stochastic modeling provides a promising approach [8–11]. Recent studies have focused on synchronization properties of node frequencies [12, 13], dynamic stability of electricity networks against perturbations [14], and influence of voltage fluctuations on frequency stability [15] and nonlocal response behavior with respect to local disturbances [16, 17]. The studies also focus on robustness against cascading failures in simplified grid topologies [18, 19], possible

curing strategies for avoidance of cascading failures [20], changes of stability under removal of transmission lines [11], finding of best locations and sizes of transmission lines for mitigating grid congestion [21] and deriving embedding solutions [22]. Here, we will partly follow the methodology of previous work by modeling the power grid with the linear power flow equations [23].

Specifically, we will study the resilience of power grids against transmission line overloads under renewable power injection at different nodes and address the following questions: How strong is the impact of the renewable generator's location on the single line overload probability and can the best locations be predicted from topological features?

Chapter 2 provides insight into today's power grids and their representation as a network. Additionally, in this chapter the standard method of power flow study is established to model power grids using the so-called power flow equations. Current toolboxes and available power grid data are presented in the final section of the chapter. Chapter 3 consists of an overview of the main renewable energy source wind and an extension of the derived power grid model that captures the fluctuating wind power properties. This method is based on the linearized power flow equations and a quasi-static response from the grid. The extended model is utilized to determine the single line overload probability of the *IEEE Reliability Test System 1996* under replacement of conventional generators by one or two wind farms. One feature that should be taken into account when integrating two or more wind farms is the spatial correlation of wind speeds at different farm locations. Therefore, we compare the two limiting cases of uncorrelated and completely correlated wind speeds. Finally, this chapter presents an outlook for further research implementing the German power grid.

Chapter 2

Modeling of power grids

This chapter develops a method to describe the complex structure of the power grid as a network and will introduce the needed basic quantities. The chapter begins with a general introduction about today's power grid regarding their structure, which are presented in section 2.1. Some general aspects and properties of network representation, including the models for nodes and edges, as well as aspects of graph theory relevant to this thesis are described in section 2.2. Section 2.3 will briefly describe the model and mathematical description of resistor and current sources according to the theory of Ohm and Kirchhoff. This theory will then be used in a power grid model that leads to the so-called power flow equations. Currently available toolboxes that implement this model and electricity grid data from real or test grids are briefly listed in section 2.4.

2.1 Information about today's power grids

Almost all of today's electrical power transport and distribution grids operate with alternating three-phase current, with a typical frequency of 50 Hz in many regions of the world and 60 Hz in America and Asia. Other electrical grids with different purposes may use other frequencies. For instance, the common frequency of the electric train operation in Germany is 16.7 Hz, while some aircraft, spacecraft, server rooms and military equipment use 400 Hz [24, 25]. For the following, more detailed, description we will focus on the German grid, the structure of which differs from other countries.

Historically the distance between generation and demand of electric power has increased, which leads to an increase in transmission voltage for lower losses. Today, a line operating under maximum capacity with 380 kV loses around 1 % per 100 km [26] and the whole German grid loses 5.7 % of the generated power [27]. The distinction between different voltage levels (see Table 2.1) originates from this development over time. We generally differentiate between the transmission system (ultra-high voltage), which transports large quantities of electric power across the country, and the distribution grid (high, medium and low voltage), which forwards the power to consumers. Sometimes the high voltage grid is also referred to as the sub-transmission grid [3]. The type and scale of production and demand varies on each voltage level, but all are connected through transformer stations.

The ultra-high voltage levels transmit power from large centralized power generators (e.g., power plants based on Uran, coal and gas as well as off-shore wind parks). There are four operators for the transmission system in Germany: 50Hertz Transmission, Amprion, TenneT TSO, and TransnetBW. These transmission grid operators (TSO)

Nominal voltage in kV	Voltage range	Application
0.23, 0.40	low voltage	small consumers, e.g. households
3-30	medium voltage	distribution in urban and rural areas
60, 110	high voltage	transmission to large consumers
220, 380, 500, 700	ultra-high voltage	long distance transmission

TABLE 2.1: Common voltage levels for the electricity transmission grid in Germany [25].

control and monitor the grid and are also responsible for the network expansion within the regulations set by federal laws. The high voltage level connects wind parks and fossil power plants, but also some large-scale consumers. Besides industrial demand, most renewable sources such as wind and water turbines, photo-voltaic and biomass are connected through the medium voltage grid. Lastly, the low voltage grid distributes the power to households and small companies. Small photo-voltaic facilities directly inject the power on this level [28]. For the whole distribution grid there are about 884 different operators [27, 29]. Table 2.1 provides an overview of the overall length

Power grid length in km	Transmission system	Distribution network	Total
total	34,855	1,763,083	1,797,938
low voltage	34,631	348	34,979
medium voltage	224	96,084	96,308
high voltage	0	509,866	509,866
ultra-high voltage	0	1,156,785	1,156,785

TABLE 2.2: Power line lengths in km for the overall grid and each voltage level separately in the year 2013 [27].

of the lines and each voltage level separately in the year 2013. The grid consist of about 1.8×10^6 km lines and 49.9 million metering points of final consumers of which 3.8 million belong to the industry [27]. The power demand of these consumers varies according to their needs and fluctuates on scales throughout day. Figure 2.1 illustrates this fluctuation for the year 2017, displaying the total load of all German transmission line operator grids. The data is obtained from the Transparency Platform [30] of the *European Network of Transmission System Operators for Electricity* (ENTSO-E). More information about the ENTSO-E and their platform appears in section 2.4. In Figure 2.1a the higher demand during the cold months is visible, as are the weekly fluctuations of 30 – 50 MW. On the monthly scale (see Figure 2.1b), the workdays have a general higher demand than the weekend with a minimal demand on Sundays. The day and night circle is clearly visible on the weekly scale in Figure 2.1c, and other than periodic behavior, there is little fluctuation. On an even smaller time scale of one day, the only change is determined by the day and night cycle, lunch break and end of work. All time windows have been chosen arbitrarily.

The electricity demand came from of different sectors in different proportions. The largest demand comes from industrial sources with 47 %; next, private households accounts for 25 % followed by trading at 15 % and others at 13 % (see the infographic in Figure 2.2b). Figure 2.2a displays the proportions of all different electric power sources in Germany in 2016. The overall amount of renewable energies is at 30 % with wind power as the leading source.

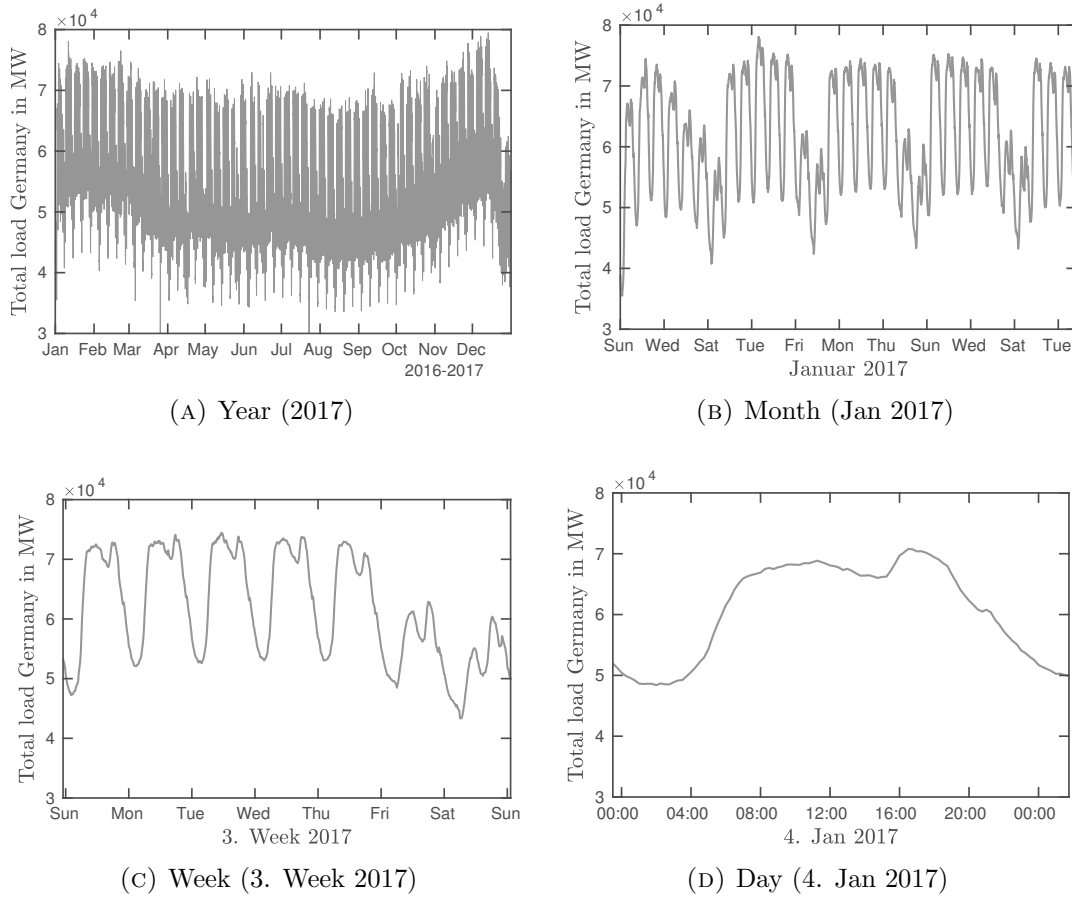


FIGURE 2.1: The total network load of the German grid in the year 2017 with a resolution of 15 minutes for different time intervals Figure 2.1a-Figure 2.1c. (Data is property of the ENTSO-E and available at their Transparency Platform [30]).

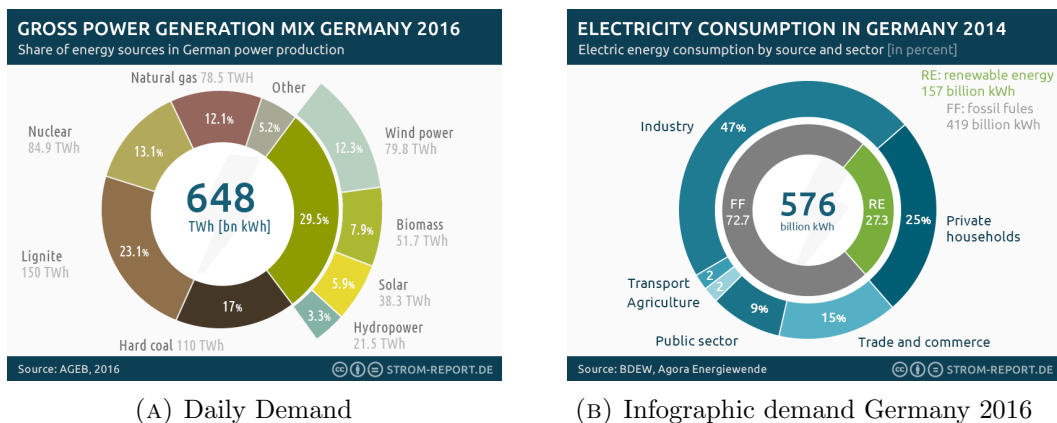


FIGURE 2.2: Infographics "Germany's power generation mix 2016": Strom-Report¹ (left) and "Electricity consumption in Germany 2014": Strom-Report (right)² [31].

¹<https://1-stromvergleich.com/strom-report/renewable-energy/#electricity-consumption-germany>
²<https://1-stromvergleich.com/strom-report/renewable-energy/#germany-power-generation-mix-2016>

2.2 Network representation

The power grid is a large system with many different components and corresponding models. Therefore one can approach the description of the power grid on different levels according to the problem being investigated. For example it is possible to describe every electronic component in small circuits, but it is unnecessary to model each component of every household when the point of interest is the electric power balance of the whole country. The common approach, therefore, is not to describe the power grid as a circuit but as a network where nodes stand for spots of power generation or consumption and edges represent power transmission. This network view presents the main structure of the power grid while allowing for modification through different node and edge models. For instance, a node could stand for one house, neighborhood, city or state. Additionally, there are many varying cable types and techniques used in the power system, which can be represented through different edge models. Figure 2.3 illustrates the topology of the *SciGRID*, which is a German power grid model developed through a research project funded by the German Federal Ministry of Education [32]. For more details, see section 2.4.

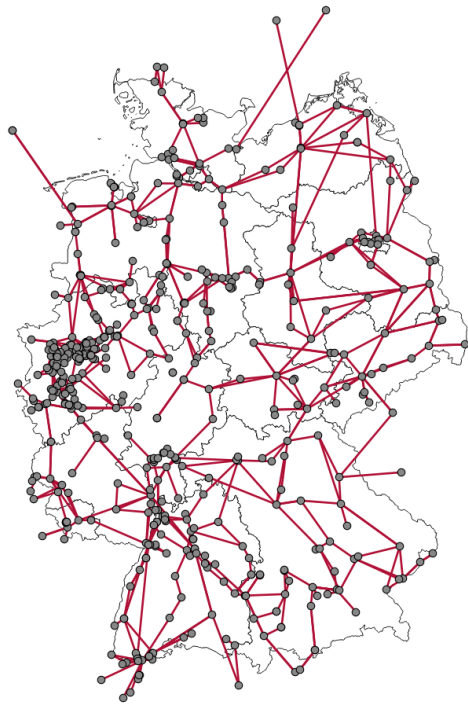


FIGURE 2.3: Example of the topology of the SciGRID network. The nodes represent substations and the edges are transmission lines with 220 – 450 kV. This network was displayed with the software QGis (see section A.8).

The structure of this section is as follows. First, the structure of the network model used in this thesis and the typical corresponding engineering terms will be explained in subsection 2.2.1. Next, the models for the nodes and edges will be described in subsection 2.2.2. Finally, subsection 2.2.3 covers some graph theory concepts that are utilized in analysis of the results later on in chapter 3.

2.2.1 Network model

A network consists of edges and nodes, as illustrated in Figure 2.3 as circles and lines. The nodes are distinct electrical points, which means a possible voltage difference and impedance between them. A finite impedance connecting two nodes corresponds to an edge in the grid. In literature, the nodes on larger scale are often called *bus*. The word bus comes from the Latin word *omnibus* (*for all*) and originates from the node structure in power grids. Multiple components are connected by a so-called *busbar*, bus for short, which can be considered as a metal bar where all incoming and outgoing wires are connected. The busbar provides a voltage reference point for all bus components. In reality there are at least three busbars, one for each phase. One bus marks the location of possible multiple generators and loads. Generator refers to a power injection into the grid and a load to a power consumption. The number of generators or loads in one node depends on the respective power grid. If the investigated power level is the transmission grid, a single load bus often represents a collection of loads and transformer connections to a sub-transmission system or distribution centers. The nodes are connected by transmission cables, where it is assumed that only one of the three phases must be considered. This one phase representation is called the one-line diagram. Engineering literature provides information and theory on the ways in which circuits can be extrapolated from one-line, or rather one phase, to three phases. Furthermore, every connection contains at least one circuit breaker as an electrical switch to protect them from overload damage, but these breakers are not outlined in the diagrams. The next typical assumption for the one-line diagram characterizes all important aspects of the lines in the impedance as the single quantity. The impedance is taken to be constant and is primarily determined by the characteristics of material, diameter, construction type and length of the cable. The ambient conditions are usually neglected for the power flow analysis and would be time dependent. Since the information about length is wrapped inside the impedance there is no need for geographical accuracy when illustrating the power grid in a one-line diagram, but it is nevertheless possible to do so [33].

2.2.2 Bus and transmission line model

The nodes represent generators and loads of the power grid, and a single node can contain multiple generators and loads. Here, the generators at node j have a power injection

$$S_j^g = P_j^g + iQ_j^g \quad (2.1)$$

and the loads a demand of

$$S_j^d = P_j^d + iQ_j^d. \quad (2.2)$$

Consequently, the total power of node j is

$$S_j = S_j^g + S_j^d. \quad (2.3)$$

Through the edges, electric power flows from node to node defined by transmission line-specific properties. To capture these properties, there are various edge models for different length, materials, size, construction, and so on.

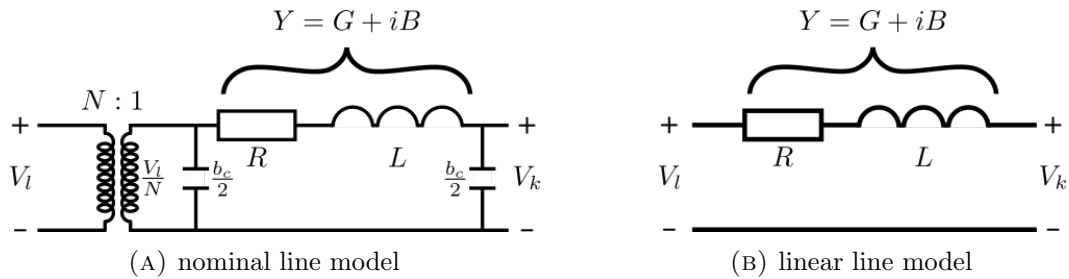


FIGURE 2.4: The nominal transformer line model (or π -model) of a transmission line (left) and the line model for the linear power flow (right).

Here we model each transmission line, transformer and phase shifter with the same branch model provided in Figure 2.4. Because the shape of the circuit resembles π , it is often called the π -model. The line consists of a series admittance y_s , an ideal phase shifting transformer and total charging susceptance b_c [34]. The line is represented through a matrix according to the currents I and voltages V of the two connecting nodes k and l

$$\begin{bmatrix} I_k \\ I_l \end{bmatrix} = Y_{br} \begin{bmatrix} V_k \\ V_l \end{bmatrix}, \quad (2.4)$$

with the branch admittance matrix Y_{br}

$$Y_{br} = \begin{bmatrix} (y_s + i\frac{b_c}{2})\frac{1}{r^2} & -y_s \frac{1}{\tau \exp^{-i\theta_{shift}}} \\ -y_s \frac{1}{\tau \exp^{i\theta_{shift}}} & y_s + i\frac{b_c}{2} \end{bmatrix}. \quad (2.5)$$

In the linearized power flow for higher voltage levels, it can be assumed $\theta_{shift} = 0$, $\tau = 1$ and $b_c = 0$ which simplifies the matrix to a susceptance branch matrix B_{br}

$$Y_{br} = \begin{bmatrix} b_s & -b_s \\ -b_s & b_s \end{bmatrix} = B_{br}. \quad (2.6)$$

The flows in the transmission lines are limited by a maximal flow or capacity P_{kl}^{\max} . Different approaches for analyzing power systems can then be implemented through different models for the lines and nodes.

2.2.3 Graph theory

The graph is an abstract representation of objects with a pairwise relation between some of the objects. These objects are called vertices (or nodes) and the connections are called edges (or lines). Formally the graph consists of a pair of sets $G = (V, E)$, such that V is the set of vertices and E a set of edges. E consists of two-element subsets of V (Figure 2.5) for an example. This model of a graph can be applied to a power system where the vertices represent generators, loads, or both, and the edges represent transmission or distribution lines, as explained in subsection 2.2.1. Generally, the edges in a graph could be directed, but in this thesis only considers undirected graphs. In the following section, only concepts of graph theory relevant to this thesis will be discussed.

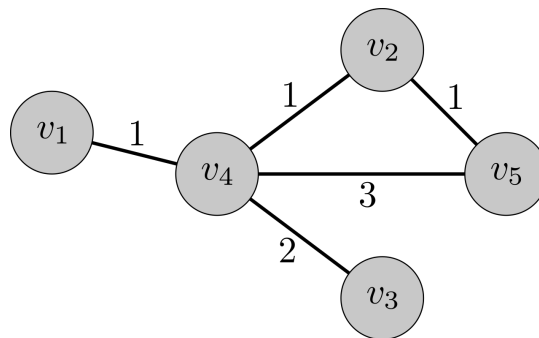


FIGURE 2.5: A simple graph of a set of vertices $V = [v_1, v_2, v_3, v_4, v_5]$ and a set of edges $E = [[v_1, v_4], [v_4, v_2], [v_2, v_5], [v_4, v_5], [v_4, v_3]]$ with weights. The graph was displayed with GraphViz (see section A.8).

Two vertices x and y of a graph G are considered to be **neighbors** or adjacent when an edge xy is a part of G . The **degree of a vertex** ($\deg(v)$) is the number of lines connected to the vertex. For example, the vertex v_5 has two connections so $\deg(v_5) = 2$. Often the average degree of the graph is important to characterize different types of graphs. One can furthermore extend the capabilities of graphs by assigning values to the edges; these numerical edge properties are often used to represent specific network characteristics and are called **weights**. The degree can also be calculated according to the weights, simply through the sum of the weights from all connecting edges. The **path** between two vertices is a trail from one node to another which contains an alternating sequence of distinct vertices and edges. For example the path from v_1 to v_3 would be $[v_1, [v_1, v_4], v_4, [v_4, v_3], v_3]$. A path can also include the weights of the edges, in which case the path then becomes weighted according to the sum of the edge weights. The example path from v_1 to v_3 has the weight of 3. The weight of a path is also often called the path **length**. Two nodes are **connected** if there is a path leading from one to the other, and entire graph is connected if there is a path between every node combination. Often one important property is the so-called **shortest path** of two nodes. The shortest path from v_i to v_j is the path with the shortest length and defines the **distance** between two nodes. There could be multiple shortest paths with the same length between two nodes.

A **network** is a specific type of graph with two sets of vertices where one set represents sources and another sinks, as well as flows through the edges. An interesting quantity is the **betweenness centrality**, which allows the important nodes in a network to be determined by the number of shortest paths that pass through a node. For example, a node in a communication network with high betweenness centrality has a high flow

of information. The betweenness centrality of a node v_k in a graph with n nodes is defined as

$$b(v_k) = \sum_{i=1}^n \sum_{j=1}^n \frac{\sigma_{ij}(v_k)}{\eta_{ij}}, \quad j \neq i, k \neq j \quad (2.7)$$

where $\sigma_{ij}(v_k)$ is the number of shortest paths from node v_i to v_j that pass through v_k and η_{ij} is the total number of shortest paths between v_i to v_j .

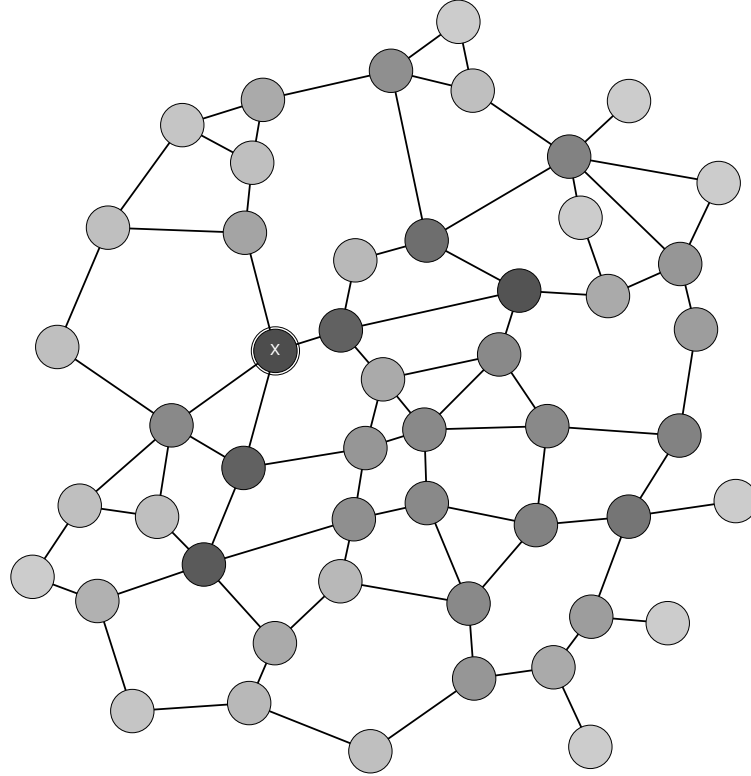


FIGURE 2.6: Illustrated is a randomly generated example network with edge weight 1. The nodes are colored according to the betweenness centrality. Dark color refers to a high and light color to a low value betweenness centrality (linear color gradient). The double circled node with the X label has the highest value.

Figure 2.6 illustrates the betweenness centrality for an example network with edge weight 1. High $b(v_k)$ corresponds to the nodes where many paths pass through whereas the outer regions and dead ends have a low $b(v_k)$. With the betweenness centrality it can be decided, that for this network the node X with the highest b is most important of the network flow.

Another interesting property is the **connectivity**, which represents the minimum number of nodes or edges that could be removed before the graph is no longer connected. There are multiple numerical algorithms used to determine the connectivity, but these algorithms will not be explored here.

2.3 Power flow analysis

Considering the large number of components, the exact mathematical model that uses electromagnetic theory for such complex systems as the power grid, is difficult if not impossible to grasp. However, experience has demonstrated that a complete knowledge of electromagnetic fields is not necessary, because only specific aspects and integral quantities of the fields are of interest. Therefore, a model for resistor networks was developed by Ohm, Kirchhoff and others, before the theory of electromagnetic field had been formulated [35]. In principle, there are two basic quantities needed to describe the flow of electricity in a network: voltage and current. In this section, the model of the power flow equations that describe power grids will be derived in subsection 2.3.1, and the corresponding analysis method explained in subsection 2.3.2.

2.3.1 Power flow equations

In this section the basics of electric circuit theory needed to derive and understand the power flow equation will briefly be covered.

One of the basic quantities is the electric current I , which is the rate of change of electric charge passing through a conductor. It is defined as

$$I = \frac{dQ}{dt} \quad (2.8)$$

with dQ the amount of electric charge that flows in time dt . The SI-unit for measuring the electric current is the *ampere*.

”The ampere is that constant current which, if maintained in two straight parallel conductors of infinite length, of negligible circular cross-section, and placed 1 metre apart in vacuum, would produce between these conductors a force equal to 2×10^{-7} newton per metre of length.” [36]

Note that the electric current has a direction. On a microscopic scale, one could define the direction through the flow of electric charge, but for the electric circuit theory this is irrelevant as long as it is consistent. Often people refer to the direction opposed to the electron movement as the technical direction, but that definition has only historical reasons.

The second physical observable needed to describe a circuit is the voltage V , defined as the electric potential Φ differences between two points

$$V = \Phi_a - \Phi_b. \quad (2.9)$$

The unit for measuring the voltage is the *volt*, which in SI base units is

$$V = \frac{kg \cdot m^2}{A \cdot s^3}. \quad (2.10)$$

The relation between current and voltage in general is represented through the (complex) impedance $Z = R + iX$ with R the resistance and X the reactance. This thesis assumes Ohm’s law with the linear connection between the voltage and current

$$V = ZI. \quad (2.11)$$

If the voltage source is constant, the resulting electric current is called a direct current (DC) with the electric power $P = VI$. The electric power P in watt is the rate of the consumed energy at one joule per second. In alternating current (AC), the voltage, and therefore the current, is periodically changing direction. The most common waveform in power systems is the sine wave. For an insight into the frequency and amplitude used in power systems, see section 2.1. In an AC circuit, the voltage and current can be shifted in time through inductivities or capacitors; the most common, abstract notation is then to describe voltage and current as complex quantities, where the shift is expressed in a phase θ .

The electric power of an AC circuit, the apparent power, is given by

$$S = I^*V = P + iQ \quad (2.12)$$

with P the real power and Q the reactive power (the asterisk denotes the complex conjugate). This description of a complex power is not intuitive and requires explanation. This explanation begins with the basic assumption that the relation $P = VI$ is always instantaneously true, so the power becomes a function of time $P(t) = V(t) * I(t)$. In power systems, a typical frequency of 50 Hz exists; however, this thesis is not interested in the power on time scales of sub seconds, but only in the effective power over many periods of voltage and current. Since the average of a sine function would be zero, one way to quantify the average quantities of voltage and current is through the root mean square (rms) value, which is $1/\sqrt{2}$ of the amplitude. For the power, this means that the average value is $P_{\text{avg}} = V_{\text{eff}}I_{\text{eff}}$, which is the same electric power as a DC current with voltage of V_{eff} and current I_{eff} . Since AC circuits contain components with reactance, there is a part of the power stored in the electromagnetic fields of coils and capacitors that is returned to the source through one complete cycle. This power is called the reactive power Q , which results from the phase difference between voltage and current [37] and does not result in a net energy transfer in contrast to the real power P . The amplitude of the apparent power is always given by

$$|S| = \sqrt{P^2 + Q^2}. \quad (2.13)$$

The unit of $|S|$ is called volt-amperes (VA) to distinguish between the real and apparent power though they have the same physical units. Now the basics necessary for the power flow equation are established [33].

For the node k of a network with n nodes, the power is defined as

$$S_k = I_k^*V_k \quad (2.14)$$

where a positive power represents generation and negative power represents consumption. The nodes are connected through transmission lines with an impedance. The line $[kl]$ connects node k and l with the impedance z_{kl} . Later, the impedance values z_{kl} will be written as a $n \times n$ matrix, where no line connection between two nodes corresponds to an infinite impedance. Therefore, for clearer notation, the inverse value, called the admittance Y ,

$$\frac{1}{Z} = Y = G + iB \quad (2.15)$$

is used. No line connection corresponds to $Y = 0$. The admittance consists of the conductance G and susceptance B . If ohmic transmission lines are assumed, it is

possible to write the current through each line from node k to l as

$$I_{kl} = (V_k - V_l)y_{kl}. \quad (2.16)$$

All voltages $V_k = |V_k|e^{i\theta_k}$ are in respect to the reference point of the ground. The ground is a neutral place (voltage zero) which can absorb currents and stay neutral. In power grid, earth acts as reservoir, because most soils are conductive and charge can disperse quickly. Power systems are specifically dug into earth and households often use metal water pipes as ground [33]. The current at node k is the sum of all currents

$$I_k = V_k \left(y_k + \sum_{l=1, l \neq k}^n y_{kl} \right) + \sum_{l=1, l \neq k}^n V_l (-y_{kl}) \quad (2.17)$$

where y_{kl} is the impedance of the line connecting node k and l and $V_k y_k$ represents the current to the ground. The current at node k can then be summarized as

$$I_k = \sum_{l=1}^n V_k y_{kl} \quad (2.18)$$

with $y_{kk} = y_k$. See appendix section A.1 for a more detailed explanation, with an example of Equation 2.18. At this point it becomes possible to describe the complete grid with Equation 2.18, however, the current is difficult to measure and mostly not known. The quantities that are known depend on the type of bus, but in general it is easy to measure the voltage in respect to the ground and power demand or consumption. The main goal is to fully describe the grid only with voltages and power. Therefore, inserting Equation 2.18 into Equation 2.14 results in

$$S_k = I_k^* V_k = V_k \left(\sum_{l=1}^N Y_{kl} V_l \right)^* \quad (2.19)$$

$$= \sum_{l=1}^N |V_k| |V_l| (g_{kl} - ib_{kl}) e^{i(\theta_k - \theta_l)} \quad (2.20)$$

$$= \sum_{l=1}^N |V_k| |V_l| (g_{kl} - ib_{kl}) (\cos(\theta_k - \theta_l) + i \sin(\theta_k - \theta_l)). \quad (2.21)$$

After multiplying, one can split Equation 2.21 into real and imaginary parts

$$P_k = \sum_{l=1}^n |V_k| |V_l| (g_{kl} \cos(\theta_k - \theta_l) + b_{kl} \sin(\theta_k - \theta_l)) \quad (2.22a)$$

$$Q_k = \sum_{l=1}^n |V_k| |V_l| (g_{kl} \sin(\theta_k - \theta_l) - b_{kl} \cos(\theta_k - \theta_l)). \quad (2.22b)$$

with $k = 1, \dots, n$. Equation 2.22a and Equation 2.22b are called the *AC power flow equations*. The power flow equations are widely used in research studies to analyze load scenarios. The required computing power for solving the non-linear equations, mostly by the Newton-Raphson method, becomes high for large numbers of nodes. Since the German power grid consists of more than 10,000 nodes, the solution takes some time (for a normal computer with standard methods this can take up to five minutes). Depending on the problem being investigated, it is often necessary to solve this equation multiple times [33].

Since the interest of this thesis corresponds to the transmission grid level, three typical approximations to the AC power flow equations can be made. The first approximation assumes that the resistance r of a transmission line can be neglected in comparison to its reactance x , $r \ll x$. This leads to

$$y = \frac{1}{z} = \frac{1}{r + ix} = \frac{r}{r^2 + x^2} + \frac{-ix}{r^2 + x^2} \stackrel{r \ll x}{=} -\frac{i}{x}. \quad (2.23)$$

which relates to a conductance $g = 0$ and susceptance $b = -\frac{1}{x}$. The second approximation assumes that the voltage phase differences between the nodes are much smaller than 1, $|\theta_k - \theta_l| \ll 1$, which linearizes the equations $\cos(\theta_k - \theta_l) = 0$ and $\sin(\theta_k - \theta_l) = \theta_k - \theta_l$. For the final approximation the voltage magnitudes $|V_k|$ are assumed constant and close to a normalized reference point of 1. Voltages close to 1 means that in multiplications the voltages can be neglected, but voltage differences remain because differences can still vary in multiple order of magnitudes. With these three approximations the power flow equations become

$$P_k = \sum_{l=1}^n b_{kl}(\theta_k - \theta_l) \quad (2.24a)$$

$$Q_k = -b_k + \sum_{l=1}^n |b_{kl}|(|V_k| - |V_l|). \quad (2.24b)$$

Equation 2.24a and Equation 2.24b are called the *linear power flow equations* often misleadingly referred to as DC power flow equations due to the linear behavior even though it is still AC current [38]. See section A.2 for an example calculation on the linear real power flow. The power flow P_{kl} through the line $[kl]$ can be calculated from Equation 2.24a by

$$|P_{kl}| = |b_{kl}(\theta_k - \theta_l)|. \quad (2.25)$$

The flow through a line is limited by the capacity $P_{kl}^{\max} = c_{kl}$.

Equation 2.24a is often written in the matrix form $\mathbf{P} = \mathbf{B}\theta$ where \mathbf{P} and θ are vectors and \mathbf{B} is the susceptance matrix with elements b_{kl} .

The susceptance matrix \mathbf{B} can be generated from the branch matrix B_{br} (see Equation 2.6) in the following way:

Each line i of n_l lines in the grid connects two buses k and l where k is the *start* bus and l the *end* bus. The $n_l \times n$ (n_l number of lines, n number of buses) connection matrix C_{start} has an element (i,k) equal to one, if the line i has the start bus k (i refers to line number, k to bus number). The $n_l \times n$ connection matrix C_{end} is defined accordingly with the l bus.

Next, the $n \times n$ susceptance matrix \mathbf{B} can be constructed

$$\mathbf{B} = (C_{start} - C_{end})^T B_{line} (C_{start} - C_{end}) \quad (2.26)$$

where B_{line} represents the diagonal $n_l \times n_l$ matrix with the line susceptance b_s^i from B_{br} as the (i,i) -th element (i refers to line number) [34].

2.3.2 Power flow study

With the derived power flow equation in subsection 2.3.1 it is now possible to describe the complete power grid. However, some parts of the equations are unknown for specific nodes and must be calculated in order to obtain the complete information. With a direct current, it is possible to determine voltage and current from each other, if the impedance is known. This means that only one quantity per node is needed in order to calculate the rest. For alternating current, the voltage angle and time-dependent magnitude are additional variables, whereby the deduction of other variables becomes more complex. The basic idea of the power flow study is to calculate the missing quantities from those that are known or measured through the power flow equations. The four variables of the power flow equation at a node are real power P , reactive power Q , voltage magnitude $|V|$ and voltage angle θ under the assumption that the admittances of the lines are known. In a grid with N nodes, the power flow equations result in $2N$ equations (see Equation 2.22a and Equation 2.22b), which are solvable with the knowledge of $2N$ of the $4N$ variables. This means that only two variables per node must be specified. In the grid, we have three types of buses defined by the different known variables: generators, loads and one slack bus. For a generator, the real power production P and the voltage magnitude $|V|$ are known and hence are called PV -buses. In general, it is also possible to the reactive power Q instead of the voltage $|V|$, but using the voltage instead is more convenient, which will be explained below. For the loads or PQ -buses, the power consumption of P and Q is known. The last bus type, known as the so-called slack bus, is an arbitrarily selected generator where the two quantities voltage magnitude $|V|$ and angle θ are known. The slack bus differs from other generators due to the special function in real power balancing and is often called the $V\theta$ bus.

Another important aspect of power flow study besides the calculation of power flow equations is the power balancing. The desired state of the system is in a power balance between all generators and demands as well as losses. This balancing applies to both the real and the reactive power.

Real power balance: If there is a mismatch in the real power balance, the system loses its synchrony, which causes failures and crashes in the worst case. To prevent this mismatch from happening the generators have to adjust to the current demand. However, most generators can scale their production accordingly to a minimum value P_{min} and P^{max} , which results in multiple production solutions for a fixed demand scenario. The limits P_{min} and P^{max} not only result from physical limits, but also from economic and political factors. One assumption therein is that the consumer demand, even with a fixed impedance, is independent from the actual bus voltage. This approximation is justified because of transformers and voltage regulators that keep the consumer voltage constant. However, finding a possible generator production solution includes not only demand but also transmission losses. Because line losses and generator production allocation are mutually dependent on each other, one encounters the loss problem. A common solution to this non-linear problem is to assume a typical line loss percentage, for example 4%, and then plan the power distribution for 104% of the demand while ignoring line losses. The assumption now is that the difference in the actual line losses is so small that only one generator needs to adjust to *take up the slack* of the remaining imbalance. This one scalable generator is the slack bus, sometimes called swing bus. The slack bus does the so-called *load-following*. If more power is consumed than produced, the generators frequency drops and increases with excess production. The frequency departure from a reference point represents a change of the voltage angle θ . A load-following generator keeps the frequency and

therefore the voltage angle constant. Since only voltage angle differences between buses are important in the power flow equations, the slack bus is often used as the reference point with the conventionally chosen value of zero.

Reactive power balance: A mismatch in the reactive balance would lead to a voltage collapse. In practice the reactive power balance is handled differently than the real power. All generators measure their voltage magnitude $|V|$ and keep it constant at all times, which corresponds to balancing a reactive mismatch. The bus voltage can be immediately measured and straightforwardly controlled. Therefore, all generators share the reactive power mismatch or *slack* and it is unnecessary to assign a *reactive slack bus*.

To summarize the balancing: a generator that keeps the voltage magnitude constant balances reactive power Q and a constant voltage angle θ refers to balance in real power P [33].

The power flow analysis is often used in finding the most efficient power distribution scenario (dispatch) or optimal power flow (OPF). The optimal power flow calculates the best solution in respect to a set of cost, security, loss and resilience criteria. The OPF algorithms often use a metric function that includes all criteria to compare multiple power flow calculation. However, the OPF solutions from such algorithms are not necessarily unique and there is no guarantee of finding the optimum solution [33].

2.4 Available grid data and toolboxes

In this section, we will shortly discuss the access to power grid data and the software used to analyze these grids. The data and models in power grid analysis are often handled restrictively by the operators and not easily publicly available. Therefore many different research projects were funded to obtain public data. There are various software and data solutions and not everything can be discussed in detail.

From the available software that analyzes power grids, the two most frequently used while working on this thesis are as follows (Information from [39]):

- MATPOWER [40] (PYPOWER) is a MATLAB based simulation package for power systems. It is developed at the Cornell University and can solve power flow scenarios as well as optimal power flow problems. It is a free open source toolbox with a detailed documentation [34]. The package PYPOWER is a port of the MATPOWER to Python. PYPOWER has an additional module for calculating dynamic problems (PYPOWER-Dynamics).
- PyPSA [41] short for "Python for Power System Analysis" is a free open source toolbox for Python and allows the simulation and optimization of power grids. It includes the following features: variable wind and solar generation, storage units, sector coupling and mixed alternating and direct current networks. Additionally, PyPSA is designed to allow calculation with large networks and long time series. PyPSA was developed as part of the *Stromnetze Research Initiative* by the Renewable Energy Group at FIAS.

See [39] for the full list of commercial and non-commercial software.

Most power system simulation software includes some example power grid data. To obtain test grids or realistic data for Germany and Europe the *Open Power System Data* platform [42] seeks to gather and publish all publicly available data. This project was developed by Europa-Universität Flensburg, DIW Berlin, Technical University of Berlin, and Neon Neue Energieökonomik. On this data platform one can find data of multiple projects that try to model power grid data based on different approaches.

Two of these projects are:

- *SciGRID* [32], which has intention to make the European transmission grid publicly available based on methods to extract data from *OpenStreetMap*. OpenStreetMap is a community-built world map containing as much data as possible. SciGRID was a project funded by the German Federal Ministry of Education and Research and performed by NEXT ENERGY - EWE Research Centre for Energy Technology.
- *open_eGo* [43], which has the goal to develop a transparent grid, but also a planning tool for grid optimization. The project is also funded through the Federal Ministry for Economic Affairs and Energy and developed by Flensburg University of Applied Sciences.

For many research problems, it is not only important to obtain the grid information but also data for load dispatches, generator properties, time series of renewable data and other time series that correspond to power systems. Here, the Open Power System Data platform has an extensive collection of data for the complete region of Europe, making it a good resource for finding the needed data.

One of the main data sources originates from the ENTSO-E [30], which represents 43 TSO's from 36 countries across Europe and aims to develop the appropriate

response to the challenges concerning the renewable energy agenda of the European governments and other modern innovations such as the smart grid. Therefore the ENTSO-E Transparency Platform was instituted. It contains the direct data from the TSO including load, generation, transmission, balancing, outages and congestion management data for multiple countries. For certain time series, like wind power and demand, the forecast is also available. However, most of the data is only available in a time resolution of 15 minutes, which is too long for certain research problems. Specifically the time series of wind velocities in short time scales is of interest. To investigate short time fluctuations a resolution of 1 Hz or higher would be optimal. For this thesis, the wind velocity data was taken from the FINO platform, which is described in section 3.1.

Chapter 3

Integration of renewable energy sources

In this section, an approach to integrate fluctuating renewable energy sources, mainly wind power, into the power grid is described. Section 3.1 provides general insight into renewable energy sources and outlines in more detail the primary renewable power of interest: wind. Section 3.2.1 integrates renewable power sources with their fluctuating property into the linear power flow description. A further extension of the model allows the probability of a single transmission line overload to be determined. Finally, in section 3.3, this model is tested to investigate the resilience of an electricity test grid, namely the *IEEE RTS-96*, against transmission line overloads for integration with one or two wind parks. In the last section, an outlook with specific ideas to utilize this method on the German power grid is illustrated.

3.1 Overview of the renewable energy source wind

The term *renewable energy* is widely used but lacks a clear definition. Here we will define renewable energy as the following:

Renewable energy sources consists of energy that is derived from natural sources which replenish themselves over short time periods. Examples of such sources are the sun, water movement (tides), wind, organic plants, waste material and geothermal heat. These sources are sometimes referred to as non-conventional energy sources. The gained energy can be directly converted to electricity or used for other applications like water heating through solar radiation or methane gas for cooking.

Non-renewable energy sources consist of energy that is derived from finite and static stocks. The sources cannot be efficiently grown or produced and are used on a scale that does not match demand. Examples are fossil fuels and nuclear power (mostly Uranium). These sources are sometimes referred to as conventional energy sources.

Most renewable energy sources originates from solar radiation such as plants and wind¹, and hypothetically if the total solar radiation at sea level could be harvested, every human would have a power supply of 20 MW². This is not possible, however, and is simply an illustration of the energy stored in renewable sources. One of the most easily accessible and environmentally friendly sources is wind [44]. Wind, along with photo-voltaics, is the primary source of renewable energy in Germany. Two problems

¹The two major factors for large-scale wind patterns are the solar heating differences between the equator and the poles as well as the planet rotation.

²An average household consumes around 2 kW.

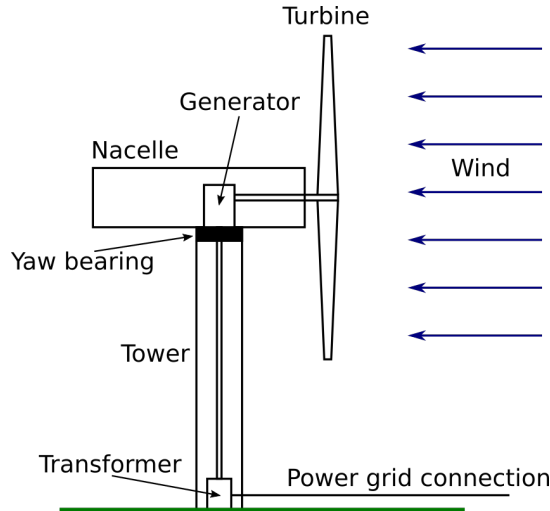


FIGURE 3.1: Shown is a typical structure of a wind turbine with the turbine, nacelle including the generator, tower, transformer and a grid connection.

with wind power are fluctuations of wind velocity and the difficulty of forecasts. In the power system industry, where everything must be planned hours in advance, this uncertainty poses a significant problem. It can be assumed that a high enough percentage of fluctuating power, accompanied by new structures, will change the system dynamics. But how is wind energy harvested? Wind turbines extract energy through aerodynamically-shaped blades that produce a lift force along the blade, which results in torque forces onto the turbine shaft. This rotation energy then is converted to electricity through a generator. A typical turbine structure is provided in Figure 3.1. Through theoretically a turbine with vertical rotation axis is possible, the more accessible structure consists of blades arranged on a horizontal axis. Three became accepted as standard, because two blades tend to produce large power pulsations and more blades interfere with each other. The produced electricity is then connected to the power grid through a transformer. The transformer is sometimes in a separate building and not placed inside the tower. Some additional subsystems are necessary, such the yaw bearing, which turns the turbine in the wind. The wind turbines located in the sea, also called off-shore turbines, have a different structure with all parts placed inside the nacelle, which is the top part of the turbine (see Figure 3.1). Moreover, in off-shore parks the power of multiple turbines is often collected at a substation before being transmitting to the mainland. This design is only an example structure, however, and there are many different schemes and power transformation techniques [3].

blades From a more theoretical standpoint the average wind power obtained from wind velocity v is

$$P = \frac{1}{2} \rho A c v^3 \quad (3.1)$$

with ρ air density, A the turbine swept area and c the performance coefficient. The terms speed and velocity are equally used, however, speed refers to the absolute value and the velocity is a vector quantity. In reality, the velocity of power conversion is a stochastic process [6]. When the wind turbine could can process the total wind energy, the wind velocity behind the turbine would be zero. This is not possible since an air flow must be continuous, but one can calculate the theoretical maximal limit of the performance coefficient, the so called Betz limit, as $c_{\max} = 0.599$. In reality the values achieve around 80 % of the Betz limit and the coefficient also varies with the tip speed. The power relation of operating turbines is consequently not a simple

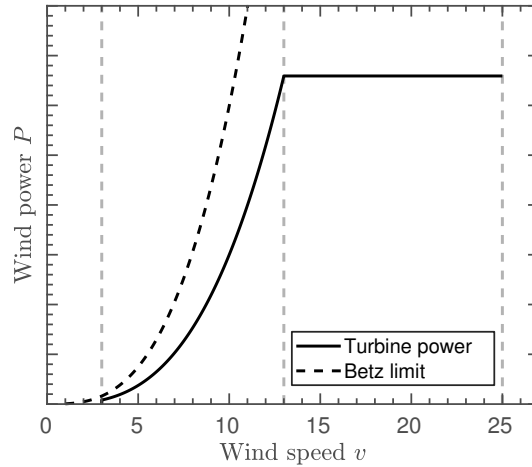


FIGURE 3.2: Typical power curve of a wind turbine as a function of wind velocity and the theoretical Betz limit.

cubic function. Figure 3.2 illustrates the typical power curve of a wind turbine and the corresponding Betz limit. For very small wind velocities the power output is too low, and the turbine will not operate. At a turbine-specific velocity, with the *cut-in speed* v_c around 3 m/s, the turbine will start operating. After this point the power will steadily rise as a function of the velocity until a *rated speed* v_r (13 m/s), where the power stays constant with increasing velocity. At high wind velocities, the turbines turn out of the wind to prevent damage at the *shutdown speed* v_s (25 m/s). A wind turbine turned away from the wind is designed to withstand wind speeds up to its *survival wind speed* (50 m/s). These values are turbine specific and often adjusted to local and economic conditions [3].

For research purposes, obtaining data of wind velocities is necessary. Often the points of interest are the wind speed fluctuations on a scale of seconds. The problem is that there are not many publicly available data sources with the frequency of 1 Hz or higher. Typically, there is only data for the average of 10-15 minutes because this is the time frame in which TSOs and wind park operators forecast wind speeds. Models of wind speed data and power conversion are still being developed in current research [45, 45–48].

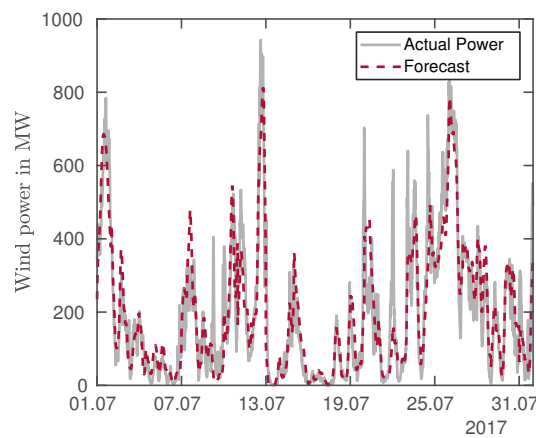


FIGURE 3.3: Wind speed forecast and actual values of the TSO TransnetBW in 15 minute steps for July 2017.

Figure 3.3 depicts the forecast of 15 minutes and the actual values of the TSO TransnetBW of July 2017. This graphs indicates that their forecast is not always correct, which results in unpredicted power mismatches. To further develop the models of wind speed fluctuations, time series with a higher frequency are needed.

Therefore, the Federal Government of Germany decided in the year 2002 to construct research platforms in the North Sea. These three platforms are called *FINO1*, *FINO2* and *FINO3*. In this thesis, data from *FINO1*, which has been in operation since 2013, will be used. *FINO1* is close to major off-shore wind parks and around 45 km north of Borkum. The location and the platform are illustrated in Figure 3.4.

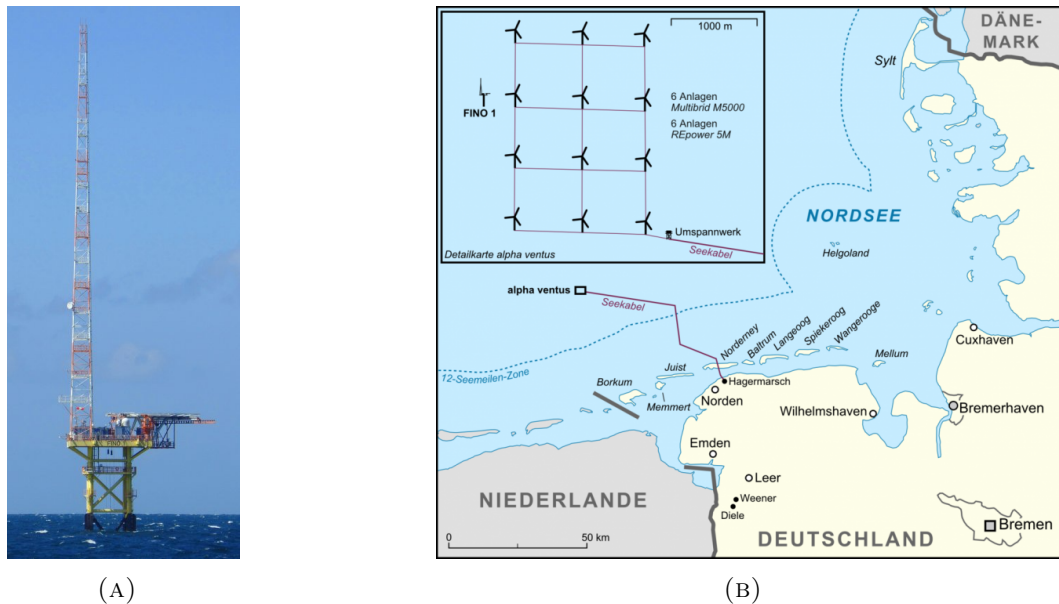


FIGURE 3.4: Shown is the location (right) and an image of the *FINO1* platform (left) ©FuE-Zentrum FH Kiel GmbH

The platform is designed to measure wind speed and direction at different heights, wave height and propagation, force of sea currents, temperature and pressure, lightning and certain ecological investigations. The wind measurement instruments are on a steel lattice constructed mast. The mast is 80 m high and the top is 103 m above the lowest astronomical tide. The anemometers are placed on brackets on the mast and one on top. Every 10 m, starting on 30 m until 90 m there are two brackets which are opposite each other. The collected data is directly transmitted to the mainland. However, the data is not always accurate, due to the influence of the mast, malfunctions, and often the impact of pollution [49].

In the following paragraph, the accessible *FINO1* data is briefly illustrated and discussed. There are other sources for not only wind speeds but multiple renewable energy sources, such as the ENTSO-E platform discussed in section 2.4. The data used here are from the anemometers with a time resolution of 1 Hz.

One aspect of wind speed data is the direction, which is often plotted in the form of a wind rose. The wind rose for the *FINO1* wind speed data at 90 m is provided in Figure 3.5. The main direction is apparent as Southwest, which as expected points towards the main land.

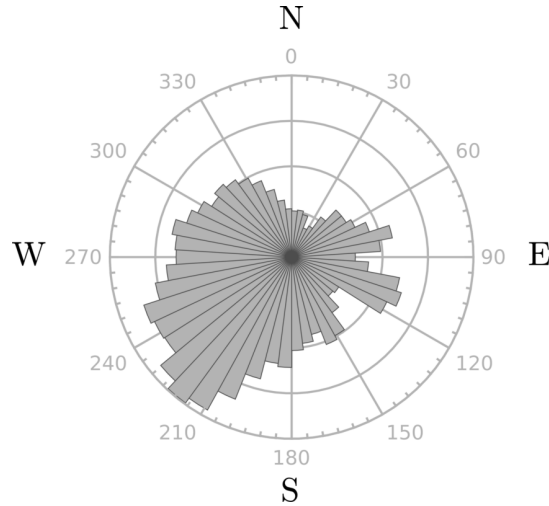


FIGURE 3.5: Wind rose of the FINO1 wind speed data at 90m.

This thesis is interested in the distribution of wind speeds and can neglect the direction, because the wind turbine turns into the wind. The histogram of a six year time series at 80 m with a frequency of 1 Hz is provided in Figure 3.6(d). The typical probability distribution for wind speeds on large time scales is the Weibull distribution with the probability density function

$$f(x; k, \lambda) = \begin{cases} \frac{k}{\lambda} \left(\frac{x}{\lambda}\right)^{k-1} e^{-(x/\lambda)^k} & x \geq 0 \\ 0 & x < 0, \end{cases} \quad (3.2)$$

where $\lambda > 0$ is the scale parameter and $k > 0$ is the shape parameter. A typical value for wind speeds is $k \simeq 2$ [50, 51]. The fitted Weibull function for the complete time series is indicated by the dashed lines in Figure 3.6(d) with the parameter $k_{fit} \approx 2.39$ and $\lambda_{fit} \approx 13.2$. However, if the distributions of ten-minute time windows are examined (see Figure 3.6(a)-(c)) the Weibull distribution is not so straightforward. For the short time frames, with only 600 data points, the distribution function may also be a Gaussian distribution with the probability density function

$$f(x; \mu, \sigma^2) = \frac{1}{\sqrt{2\pi\sigma^2}} e^{-\frac{(x-\mu)^2}{2\sigma^2}}, \quad (3.3)$$

where μ is the mean, σ the standard deviation and σ^2 the variance. For comparison Figure 3.6 illustrates the Weibull and Gaussian fit for the total time series and for three example ten minute time windows. The parameters for the total series are $\mu_{fit} \approx 11.1$ and $\sigma_{fit} \approx 5.49$.

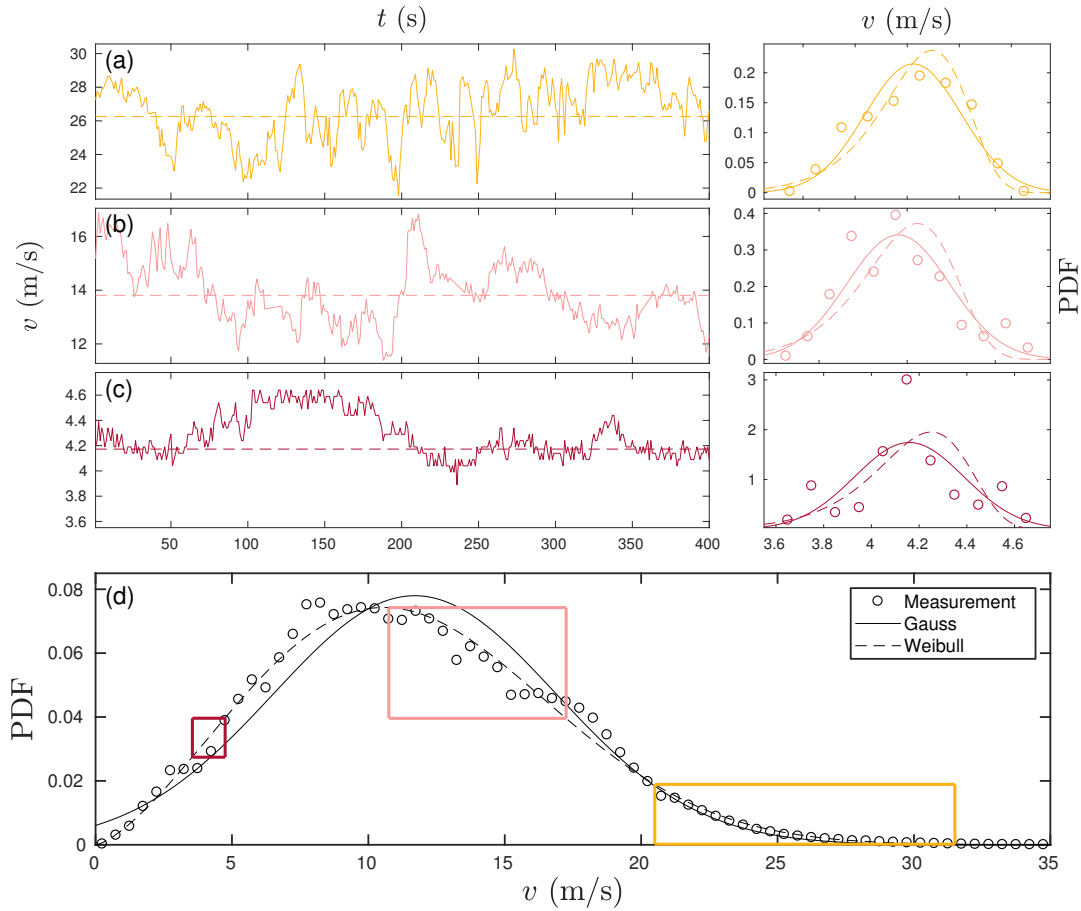


FIGURE 3.6: (a)-(c) Three example time series of ten-minute windows and their probability distributions with a Gaussian (line) and a Weibull fit (dashed). (d) The distribution of the total time series of six years on 80 m with Weibull and Gaussian fit. The location of the ten minute time windows is marked by the corresponding colored rectangles in the total distribution.

Besides the uncertainty about the correct distribution function, an interesting observation in Figure 3.6 is the scaling of the fluctuations with the average of the time window. For higher wind speeds in Figure 3.6(a) the fluctuations range 8 m s^{-1} , while for the lowest speeds in (c) they span only 0.8 m s^{-1} . This is also illustrated by the length of the rectangle in the total distribution. The remainder of this thesis assumes that the Weibull distribution is accurate enough and captures the key elements of the wind fluctuations.

3.2 Modeling renewable sources in the power grid

3.2.1 Fluctuating sources in the linear power flow

Due to the fluctuating nature of wind, the question arises on how to treat wind and other renewable sources, such as solar radiation, in power grid analysis. In section 2.3, the power flow equations and their common method of analyzing power grids is established and will be further expanded in this section. There the linearized real power flow equation (see Equation 2.24a) will be used to describe our grid. This linearization means that every node k in the network has the power $P_k = P_k^d + P_k^g$, with P_k^d the demand and P_k^g the production at the node. Furthermore, a method will be presented to determine if the grid is in a stable state in respect to a single transmission line overload.

With the assumption that the power grid is in a steady state, in which the generators match the total demand, it is assumed that the wind power fluctuations occur on short a time scale compared to those of loads, and a long time scale compared to the time needed for power adjustments of the conventional generators. The system is in a quasi-static state [23]. To maintain the balance of power, conventional generators react to the mismatch created by the power fluctuations. This reaction is captured in a common factor γ for all conventional generators, which models the primary regulation response with

$$\gamma = \frac{\sum_{j=1}^{n_d} P_j^d - \sum_{l=1}^n g_l}{\sum_{k=1}^{n_g} P_k^g}, \quad (3.4)$$

where n_d is the number of loads, n_g the number of conventional generators and n the number of wind farms with production g_l . Next, the linearized power flow equation is used while the renewable sources are treated as variables. The phase angles from the solutions of Equation 2.24a then become linear functions of the wind powers g_l ,

$$\theta_j = \alpha_j + \sum_{l=1}^n \beta_{jl} g_l, \quad j = 1, \dots, N-1, \quad (3.5)$$

with coefficients α_j and β_{jl} depending on the P_j^d , P_j^g and the set of susceptances of the transmission lines.

The stability of the grid is evaluated by its resilience against transmission line overload. All transmission lines are limited by a maximum capacity P^{\max} . For the line connecting nodes k and l , the capacity P_{kl}^{\max} limits the flow in the line $|P_{kl}|$, which can be calculated through the angles and the line susceptance b_{kl} as

$$|P_{kl}| = |b_{kl}(\theta_k - \theta_l)|. \quad (3.6)$$

The power grid is only in a stable or feasible condition if $|P_{kl}| < P_{kl}^{\max}$ is fulfilled. Inserting the solutions from Equation 3.5 one can determine the resulting feasible region in the n -dimensional Cartesian space \mathbb{R}_+^n spanned by the wind powers g_l . For each line the region is bounded by the two limiting planes.

$$(\alpha_k - \alpha_l) + \sum_j^n ((\beta_{kj} - \beta_{lj})g_j) = \pm P_{kl}^{\max} / |b_{kl}| \quad (3.7)$$

These conditions define a convex n -polytope around the origin of wind power space (with $g_l > 0$). If one wind power configuration lies outside this polytope, at least one

transmission line is overloaded. If only one wind farm is connected to the grid, the one dimensional feasible space is a line with a critical value g_k^c . For two dimensions the polytope results in a polygon \mathcal{P} . An example calculation of obtaining polygons in an example grid is provided in section A.3.

3.2.2 Statistics of line overload probabilities

One aspect of the integration of wind power is knowing the statistic of the fluctuations. However, the description of wind speed and power is difficult to capture, since it not only requires a good model for the wind speed but also for the additional process of transforming wind speed into power. In this thesis the description of wind speed is based on well-known findings for the distribution of wind velocity. The Weibull function $\mathcal{W}(v; k_v, \lambda_v)$ sufficiently represents the wind speed v , as discussed in section 3.1, with the typical shape parameter value of $k_v \simeq 2$. λ_v is the scale parameter and depends on the location of the wind farm. However, for this research the value of λ_v is not of interest because it is used to scale the wind farm size. To model the wind power, the average relation of the power curve $g \propto v^3$, is used (see section 3.1). Since this relation is a monotone function, it is possible to calculate the probability density function $\rho(g)$ from the Weibull function $\mathcal{W}(v; k_v, \lambda_v)$. The calculation is performed in section A.4 and results in

$$\rho(g) = \mathcal{W}(v^3, k_v/3, \lambda_v^3), \quad (3.8)$$

which means that the wind power is also Weibull distributed with the shape parameter of $k_g = k_v/3$. The scale parameter λ_g can be used for scaling the wind farm size. With the known probability density function of the wind power and the feasible region from subsection 3.2.1, it becomes possible to calculate the line overload probability Π of leaving the feasible region. If one wind farm is present in the grid, the probability is straightforward

$$\Pi = 1 - \int_0^{g^c} dg \rho_1(g) = 1 - \int_0^{g^c} dg \mathcal{W}(g; \frac{2}{3}, \lambda_g) = \exp \left[- \left(\frac{g^c}{\lambda_g} \right)^{2/3} \right], \quad (3.9)$$

with the critical production value of g^c limiting the one dimensional feasibility region. For two integrated wind farms, with a joint probability distribution $\rho_2(g_1, g_2)$, the equation will be

$$\Pi_{ij} = 1 - \int_0^\infty dg_1 \int_0^\infty dg_2 I(g_1, g_2) \rho_2(g_1, g_2), \quad (3.10)$$

where $I(g_1, g_2)$ is the indicator function of the feasibility region \mathcal{P} , with $I(g_1, g_2) = 1$ if $(g_1, g_2) \in \mathcal{P}$ and zero otherwise. Having said this, if two or more wind farms are integrated, their wind speeds can not be assumed to be spatially uncorrelated as recent research has shown [46–48]. Therefore, the joint probability distribution $\rho_2(g_1, g_2)$ needs to be specified. To investigate the influence of correlations on the line overload probability, this thesis will distinguish between the two extreme cases of uncorrelated wind speeds and completely correlated wind speeds. The uncorrelated case has the joint probability distribution of

$$\rho_2(g_1, g_2) = \mathcal{W}(g_1; \frac{2}{3}, \lambda_1) \mathcal{W}(g_2; \frac{2}{3}, \lambda_2), \quad (3.11)$$

where λ_1 and λ_2 represent each wind farm size. In the completely correlated case both wind farms have equal wind speeds and given a reference power g_0 from a wind turbine,

both farms produce power corresponding to their sizes $g_1 = \lambda_1 g_0$ and $g_2 = \lambda_2 g_0$. For example, location one contains three more turbines than in location two, which results in more power at the same wind speeds in respect to the λ_1/λ_2 relation. This relation assumes that at both locations the transformation from speed to power is the same. This dependency can be summarized in the constraint $g_2 \lambda_1 = g_1 \lambda_2$ which implies that the conditional probability of one is given by the other with $\rho_{1,i}(g_i|g_j) = \delta(g_i - g_j \lambda_i/\lambda_j)$. This results in the joint probability of

$$\rho_2(g_1, g_2) = \rho_1(g_1) \rho_{1,2}(g_2|g_1) = \mathcal{W}(g_1; \frac{2}{3}, \lambda_1) \delta(g_2 - g_1 \lambda_2/\lambda_1). \quad (3.12)$$

Note that in the correlated case the indicator function $I(g_1, g_2)$ can be simplified to a critical value g^c , because the ratio λ_1/λ_2 defines a line in the g_1 - g_2 space. This line crosses the feasible region \mathcal{P} at the critical value g^c . Therefore, the completely correlated wind speeds of two wind farms can be viewed as a one-dimensional problem, as with the single wind farm, and solved analytically. The uncorrelated case is solved numerically with the integrated MATLAB function *integral2()* and is described in more detail in section A.5.

One can extend the problem with the condition, that the wind farms produce a fixed total average power $\overline{g_{tot}}$ and an accordingly scaled λ . This λ is not as straightforward as taking the mean of the Weibull function to calculate $\lambda = \frac{\overline{g_{tot}}}{\Gamma(1+1/k)}$, because only the feasible region contributes to power production. For one node this results in the condition

$$\begin{aligned} \overline{g_{tot}} &= \int_0^{g^c} dg \rho_1(g) g = \int_0^{g^c} dg \mathcal{W}(g; k, \lambda) g \\ &= \lambda^{\frac{1}{k}} \Gamma\left(\frac{1}{k} + 1, \left(\frac{g^c}{\lambda}\right)^k\right), \end{aligned} \quad (3.13)$$

with $\Gamma(\cdot, \cdot)$ as the incomplete Gamma function [52]

$$\Gamma(a, x) = \int_0^x y^{a-1} e^{-y} dy. \quad (3.14)$$

Therefore, to calculate the correct scaling factor λ for a fixed amount of average power $\overline{g_{tot}}$, one has to solve the integral Equation 3.9 under the constraint Equation 3.13. For two nodes the constraining integral becomes

$$\overline{g_{tot}} = \int_0^\infty dg_1 \int_0^\infty dg_2 I(g_1, g_2) \rho_2(g_1, g_2) (g_1 + g_2). \quad (3.15)$$

Since there exist multiple combinations of wind farm sizes that correspond to the same average power, this thesis will optimize for the single combination of λ_1 and λ_2 with the smallest overload probability. For the correlated case, this optimization can be simplified with the one-dimensional view as discussed above. The best pair of λ is simply defined by the longest distance between the origin and the feasibility region boundaries. For a convex polygon, the farthest point is always one of the corner points. The numeric method of solving the optimization for two nodes is presented in section A.5 and is based on the MATLAB Interior Point algorithm *fmincon* [53].

3.3 IEEE test grid resilience against wind power injection

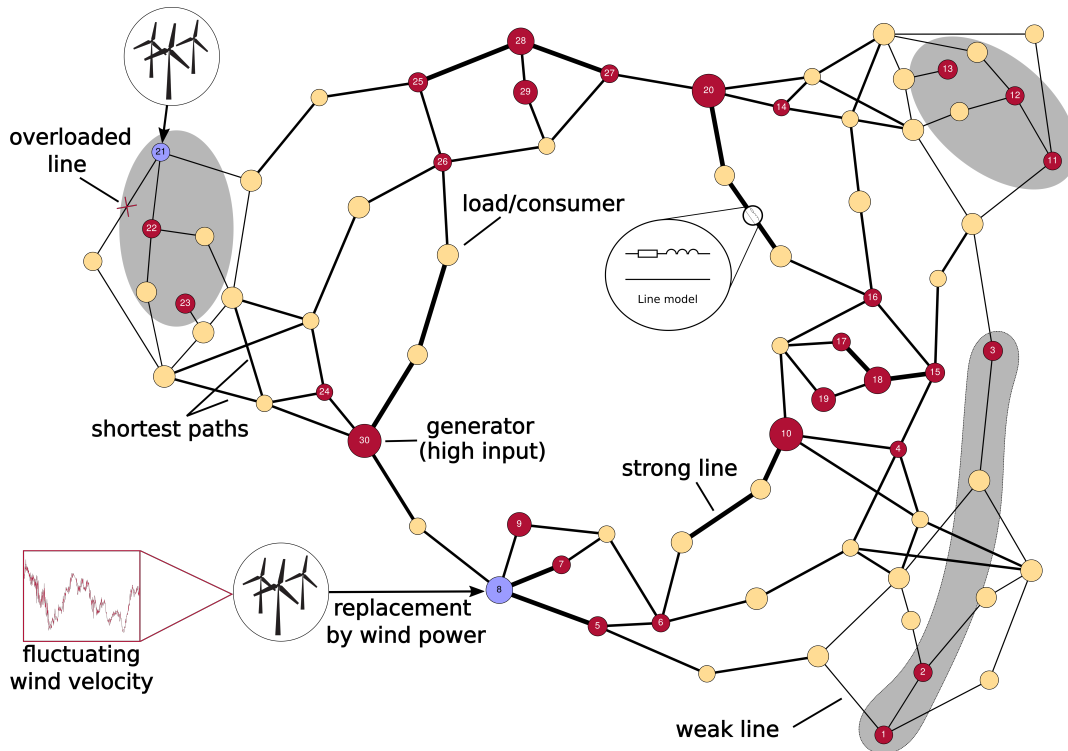


FIGURE 3.7: The IEEE RTS-96 test grid with 30 generators (red) and 53 loads. They are connected through 108 transmission lines. One or two generators are replaced by fluctuating wind farms (blue nodes), which may result in an overloaded line. The gray markings refer to regions with a high overload probability for the single generator replacement, see Figure 3.8.

Some of the following results and figures in this section have already published in [54] and some passages have been quoted verbatim.

In this section, we study how wind power integration at different nodes affect grid stability against overloads of transmission lines. Specifically we address the following question: If a given amount of conventionally generated power is replaced by wind power, where are the most favorable locations for wind farms, if single line overloads are to be avoided?

To answer this question, we used the developed power flow model for the steady state system with integrated renewable energy sources from subsection 3.2.1. We applied this model to the *IEEE Reliability Test System 1996* (IEEE RTS-96), which was developed for comparative and benchmark studies [55]. The test grid provides 15 tables of data, while section A.6 indicates which table was relevant to our research and how we converted them. The IEEE test grid data contains realistic power production and demand values for a typical situation of 73 nodes, of which 30 have a power generator. All nodes are connected through 108 transmission lines with different admittances and capacities. The methodology of the approach is illustrated in Figure 3.7. First, we addressed the question of how strongly the overload probability varies for different wind power injection locations if one generator is replaced with a wind farm. We then studied how simultaneous replacement of two conventional generators at different nodes affect the probability of line overloads. For both cases the wind farm (or farms)

should replace an average production of $g_{tot} = 200$ MW, which corresponds to a power production of a mid-sized wind farm and is also a typical power production of an individual conventional generator in the test grid.

3.3.1 Embedding of a single wind farm

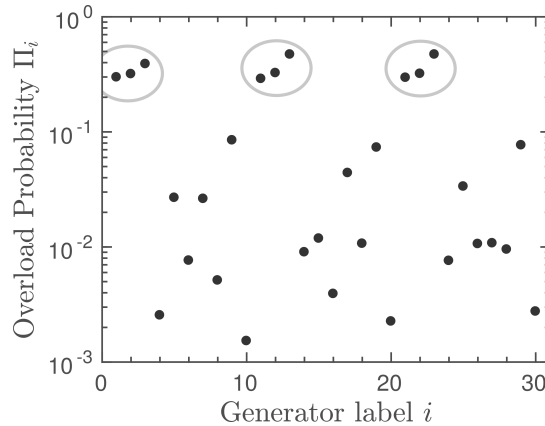


FIGURE 3.8: Line overload probabilities Π_i for wind power injection at generator node i with an average power production $g_{tot} = 200$ MW. Encircled are the three most vulnerable regions with the highest overload probability.

In this subsection the case of a single generator replacement will be considered. This case results in 30 possible different locations for an embedded wind farm. If a single node i is replaced, the feasibility region $[0, g_i^c]$ is defined through the critical power g_i^c . As long as the wind farm injects power $g \in [0, g_i^c]$, no condition is broken and no line overload occurs in the grid. If the wind power g_i exceed the critical power g_i^c , at least one transmission line overloads. Figure 3.8 contains the calculated overload probabilities Π_i for the IEEE test grid, when replacing each conventional generator i individually. The overload probabilities Π_i vary by more than two orders of magnitude dependent on the location, showing that the protection against line overload can be an important factor for optimizing wind power embedding into existing grids. Furthermore one can identify three regions of vulnerable nodes with a high overload probability compared to other locations, which are marked by the circles in Figure 3.8. The location of these nine generators in the test grid are marked in Figure 3.7 by the gray regions. These regions could be observed as the *outer* parts of the grid, but the grid is illustrated without taking coordinates or length into consideration. Nevertheless one can suspect, that the outer parts of the illustrated grid have different topological properties than the rest. We found two structural features of the nodes to be particularly relevant for the magnitude of the associated overload probabilities.

First, excess production should be more easily distributed, if there are many high capacity lines in the immediate neighborhood of the wind farm. This feature is captured in the capacity-weighted node degree (see subsection 2.2.3) of the wind farm and shown in Figure 3.9. A linear correlation between the logarithm of the overload probability and the capacity-weighted node degree is visible, but not distinct for the nodes with a higher degree. This relation results in a Pearson correlation coefficient of -0.922. Another feature that could be relevant is the betweenness centrality (see subsection 2.2.3) of the wind farms. A high betweenness centrality corresponds to a high number of shortest paths that travel through the node. However, page 32 demonstrates that the capacity-weighted betweenness centrality has no visible

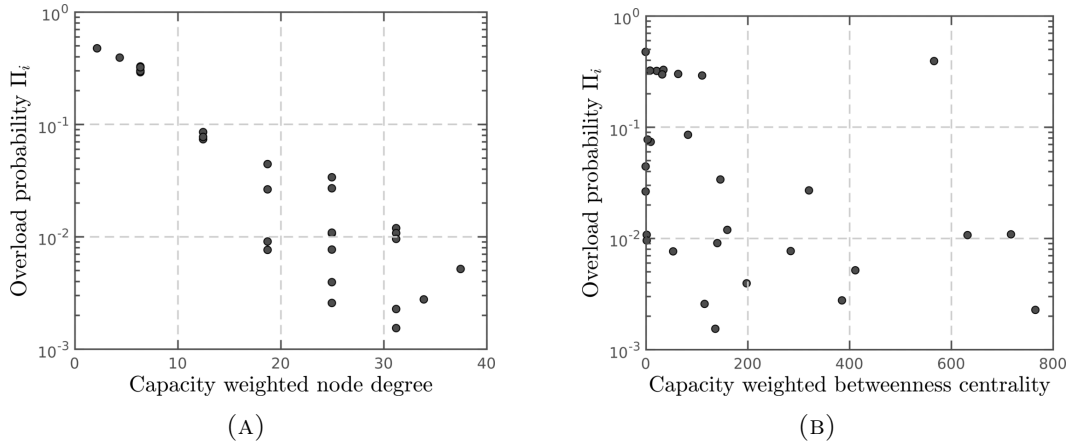


FIGURE 3.9: The overload probability Π_i for single node i replacement with the corresponding capacity weighted node degree (left) and the capacity weighted betweenness centrality (right). Note that both plots are shown in a double logarithmic scale and the degree is in units of 100 MW.

correlation to the overload probability. Furthermore, there are no improvements to the correlation coefficient with the unweighted attributes (see section A.7).

Secondly, conventional generator nodes in the neighborhood of the wind node can help to stabilize the grid against line overload, because their regulated response implies a decrease of their power supply in the environment of the wind node upon the increase of injected wind power. The most vulnerable nodes with high Π_i in Figure 3.8 have at most one conventional generator as a neighbor.

3.3.2 Embedding of two wind farms

If two generators at nodes i and j are replaced through wind farms with power g_1 and g_2 , the feasibility regions are polygons \mathcal{P}_{ij} , where the grid is only stable if $(g_1, g_2) \in \mathcal{P}_{ij}$. Since there are 30 generators in the IEEE grid, we have 435 distinct pairs of generator replacement possibilities. The form and characteristics of these polygons are provided in Figure 3.10 with some representative examples and will be discussed below. All polygons are displayed in Appendix B. The large polygon corresponds to the feasibility region if the wind farm injects wind power at $i = 1$ and $j = 2$.

If the wind power g_1 and g_2 passes one of the edges of the feasibility region, the power flow in at least one edge exceeds its capacity and an overload occurs. The two coordinate axes cannot be passed, since wind power is only positive with $g_2 \geq 0$ and $g_1 \geq 0$. Every edge of the polygon correspond to the specific constraint of one line $[kl]$ connecting two possible other nodes k and l . For the example polygon \mathcal{P}_{12} , this correspondence means that there are three lines that could be passed, and the edge with the indicated length $l_{ij}^{[kl]}$, for example, connects node 1 with a neighboring load. In subsection 3.2.2, we explained, that two completely correlated wind farms can be reduced to a one-dimensional problem, under the assumption that the wind farms are scaled in an optimal way. Here the optimal scaling point, or rather the optimal ratio λ_1/λ_2 , is defined by the longest distance to the origin, indicated by the line l_c in Figure 3.10.

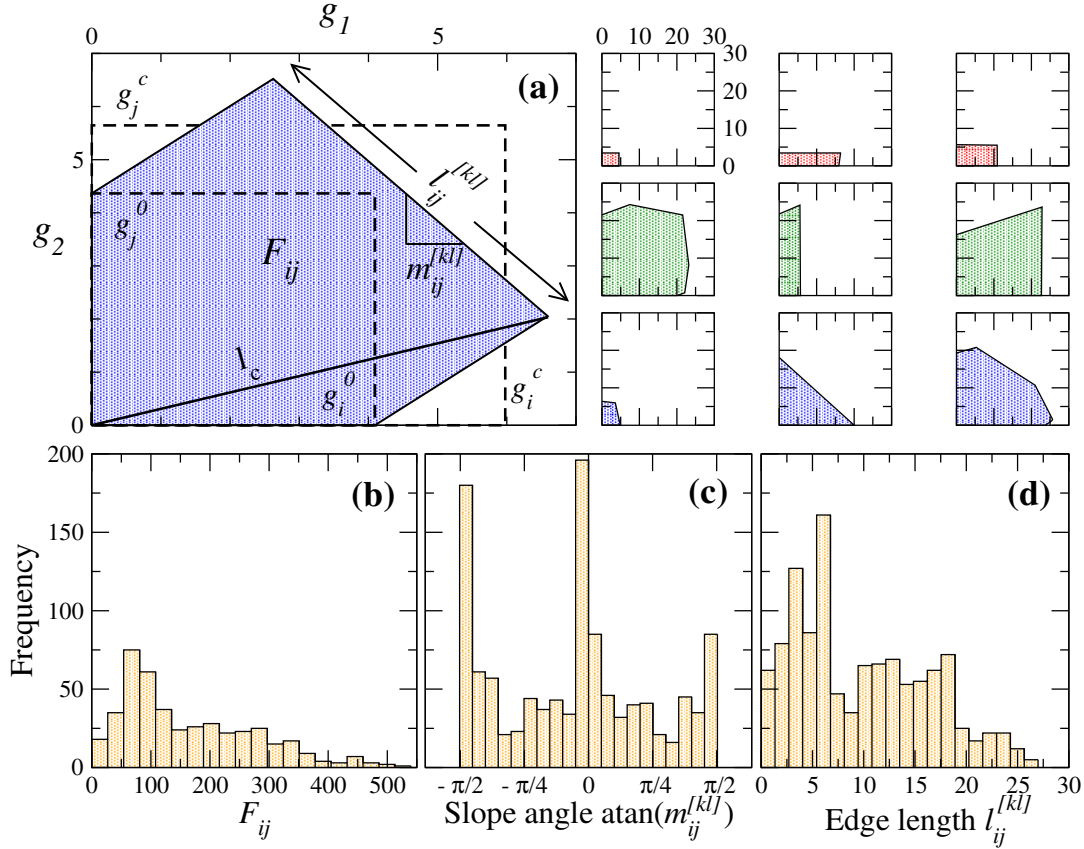


FIGURE 3.10: (a) An example of the resulting polygons \mathcal{P}_{ij} in units of 100 MW. On the left side the polygon \mathcal{P}_{12} with the wind node pair $i = 1$ and $j = 2$ is shown. Every point inside the blue area F_{ij} refers to a feasible point. The polygon edge refer to line overloads, where the edge corresponding to the line overload from node k to node l has the length $l_{ij}^{[kl]}$ and slope $m_{ij}^{[kl]}$. The two dashed rectangles and the line l_c are drawn for comparison (see text). On the right side 9 examples for three different topological distances $L_{ij} = 3$ (lower row), $L_{ij} = 5$ (middle row) and $L_{ij} = 7$ (upper row) are arranged. (b)-(d) Histogram of (b) all polygon areas F_{ij} , (c) all slope angles of all polygons with $\text{atan}(m_{ij}^{[kl]})$ and (d) all polygon edge lengths $l_{ij}^{[kl]}$.

Figure 3.10 shows that not only can the areas F_{ij} of the polygons \mathcal{P}_{ij} be quite different, but also the number of confining edges and their slope.

First, let us consider the area F_{ij} . The histogram of all 435 areas F_{ij} is provided in Figure 3.10(b), which displays a broad unimodal distribution with the mode at about $(800 \text{ MW})^2$. The large spread of areas implies strong variations of overload probabilities, since F_{ij} gives a rough measure for the overload probability because a small area corresponds to high scaling factors λ_i and/or λ_j to match the desired $\overline{g_{tot}}$. This presumption is confirmed in Figure 3.11, where the overload probability of both the correlated and uncorrelated case are illustrated in a double logarithmic scatter plot against area F_{ij} .

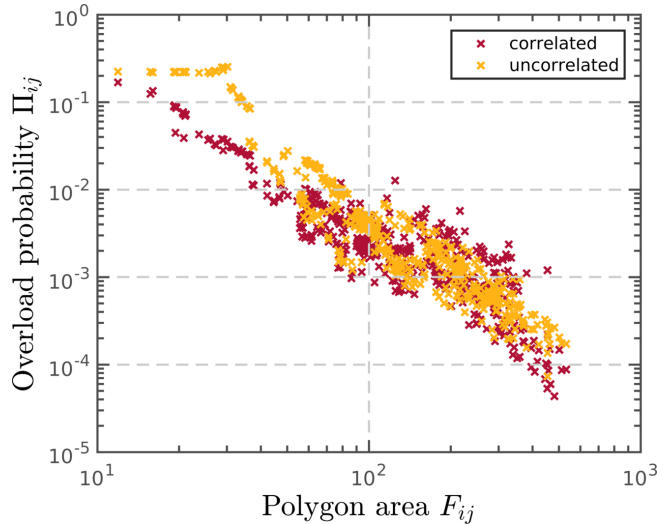


FIGURE 3.11: Overload probability Π_{ij} of all possible 435 pairs against the corresponding polygon area F_{ij} on a double logarithmic scale. F_{ij} is in the units of $(100 \text{ MW})^2$.

The expected tendency is visible for both cases, but a difference for high overload probability is also visible. This difference can be easily explained as follows. A polygon with the form of a rectangle (for example, the middle polygon in Figure 3.10) will have a long distance to the outermost point of the polygon, which defines the overload probability in the correlated case, but a small fluctuation in the short direction of the rectangle causes an overload.

The shape of the polygons, mainly the slope, provides interesting information on the influence that the two wind nodes have on each other. If wind power injection at one node would not affect the critical power at the other, the polygons become simple rectangles. For comparison, two of such virtual rectangles $[0, g_i^0] \times [0, g_j^0]$ and $[0, g_i^c] \times [0, g_j^c]$ are indicated by the dashed lines of the polygon drawn in Figure 3.10(a). Here, the value g_i^0 is the critical value for power injection at node i , if no power is generated at node j , and g_j^0 has the analogous meaning. The value g_i^0 differs from the critical value g_i^c for single node injection, because the latter refers to a situation in which there is a nonzero amount of conventionally generated power at node j . Another example is the third green polygon in Figure 3.10, which has one vertical edge and one with a small slope. The vertical line means that the limit at one node is independent of the other, as discussed above. For the other line a change of injected wind power in the horizontal axis would change the threshold of the other wind farm. Also possible is a polygon with only one edge, as in the second blue polygon. Here the wind farms have the same mutual influence.

The nine smaller polygons in Figure 3.10 refer to three polygon examples for three fixed different topological distances L_{ij} from node i to j , with $L_{ij} = 3$ in the lower row, $L_{ij} = 5$ in the middle row and $L_{ij} = 7$ in the upper row. With an increasing topological distance L_{ij} between the wind nodes, interactions decrease and the polygons tend to exhibit a more rectangular shape.

More detailed information on the correlations can be inferred by analyzing the edges and slopes of the polygons. The slope $m_{ij}^{[kl]}$ of an edge, or the corresponding slope angle $\text{atan}(m_{ij}^{[kl]}) \in [-\pi/2, \pi/2[$, is a measure for the wind node coupling with respect to the overload of the line $[kl]$. Slope angles near zero (nearly horizontal edge) and $(\pm\pi/2)$ (nearly vertical edge) and a change of power at one injection node have almost

no effect on the threshold power for line overload at the other node. Additionally, there are two possible cases in which the slope is either positive or negative, from which different couplings result. A negative slope indicates that an increase of wind power at one of the injection nodes decreases the threshold power at the other injection node for the overload of line $[kl]$. A positive slope means that an increase of wind power at one node increases the threshold power at the other node, which stabilizes the grid. In both events one can say that the wind node exhibits a positive or negative coupling with respect to the overloaded line $[kl]$.

This seemingly paradoxical behavior of positive coupling results in the possible compensation of the power flows along the transmission lines. In addition, an increase of wind power leads to an adjustment of all conventional generators, which might be in the neighborhood of the other wind farm.

A node with only positive coupling is not possible, since one positive slope cannot set the boundaries for a convex polygon with the two axes. This restriction means that every node pair has at least one negative coupled line.

Mathematically, the slope $m_{ij}^{[kl]}$ for the overload of line $[kl]$ under wind power injection at nodes i and j follows from the solution of the linear power flow equations after the replacement of conventional generator nodes. If Equation 3.7, defining the line $[kl]$ of the polygon, is written down for two wind farm locations i and j

$$(\alpha_k - \alpha_l) + ((\beta_{ki} - \beta_{li})g_i + ((\beta_{kj} - \beta_{lj})g_j = \pm P_{kl}^{\max}/|b_{kl}| \quad (3.16)$$

one can obtain the slope from these coefficients with

$$m_{ij}^{[kl]} = \frac{\beta_{ki} - \beta_{li}}{\beta_{lj} - \beta_{kj}}. \quad (3.17)$$

Figure 3.10(c) presents the histogram of all slope angles $\text{atan}(m_{ij}^{[kl]})$, which displays maxima at zero and $(\pm\pi/2)$ corresponding to horizontal and vertical edges. The whole histogram indicates a symmetry around zero with minima at the maximum coupling angles of $(\pm\pi/4)$.

The histogram of the edge length $l_{ij}^{[kl]}$ is displayed in Figure 3.10(d) and indicates a wide spread in the range of 100 – 2000 MW without characteristic signatures. Closer inspection of the distribution of the slope angles in dependence of the distances L_{ij} between the wind nodes reveals that strong node couplings with $\text{atan}(m_{ij}^{[kl]}) \simeq \pm\pi/4$ occur only for sufficiently small L_{ij} . This result is provided in Figure 3.12(a), where all angles $\text{atan}(m_{ij}^{[kl]})$ are plotted against the topological distances L_{ij} . With increasing L_{ij} , the angle distribution separates into two peaks around zero and $(\pm\pi/2)$. Overall, the couplings become smaller with increasing distance L_{ij} .

Furthermore, since positive coupling may be caused by flow compensation of the wind nodes, we expect positive slopes to be more likely the closer the overload line lies to the shortest path. To quantify this feature, we introduce the following measure for the distance of the link $[kl]$ to the shortest path connecting nodes i and j :

$$L_{ij}^{[kl]} \equiv \min(L_{ik}, L_{il}) + \min(L_{jk}, L_{jl}) + 1 - L_{ij}. \quad (3.18)$$

This measure corresponds to the excess length when subtracting the distance L_{ij} from the length of the path connecting nodes i and j via link $[kl]$, illustrated in Figure 3.12(b). For a line $[kl]$ that belongs on the shortest path between i and j this measure becomes $L_{ij}^{[kl]} = 0$.

In Figure 3.12(b) the slope angles $\text{atan}(m_{ij}^{[kl]})$ are plotted against the newly introduced

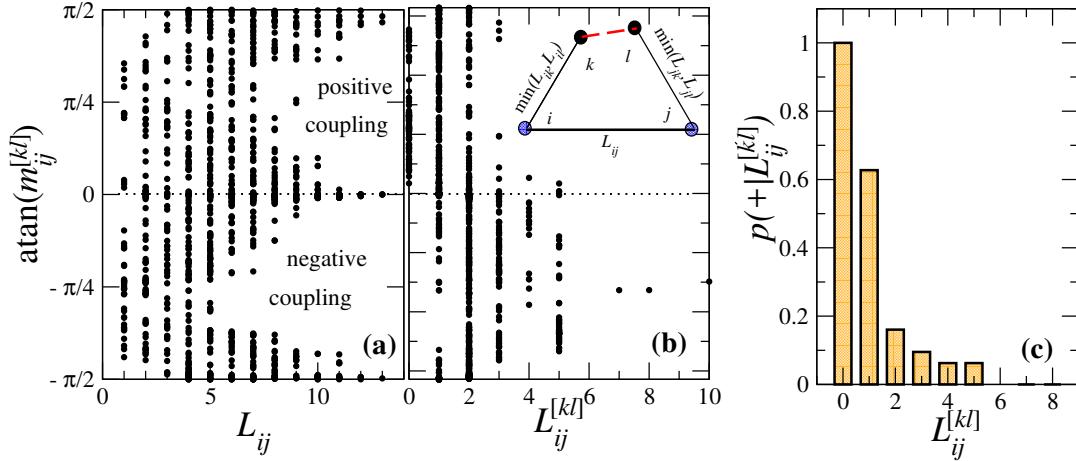


FIGURE 3.12: Plots of the slope angles $\text{atan}(m_{ij}^{[kl]})$ versus (a) the topological distance L_{ij} between the wind feeding nodes i and j , and (b) the distance $L_{ij}^{[kl]}$ of the overloaded line $[kl]$ from the shortest path connecting the wind nodes. (c) The probability $p(+|L_{ij}^{[kl]})$ of finding a positive (+) node coupling under the condition of given $L_{ij}^{[kl]}$ is shown in dependence of $L_{ij}^{[kl]}$.

distances $L_{ij}^{[kl]}$. Positive coupling can be found for every overloaded line, that belongs to the shortest path. The number of positive node couplings decreases for a higher distance $L_{ij}^{[kl]}$. In Figure 3.12 the probability of finding positive coupling $p(+|L_{ij}^{[kl]})$ under the condition of a given $L_{ij}^{[kl]}$ is illustrated. The probability rapidly decreases from one to zero at $L_{ij}^{[kl]} = 6$. Finally, we analyze the impact of spatial correlations between the wind powers at the injection nodes on the line overload probabilities Π_{ij} calculated according to subsection 3.2.2. To compare the uncorrelated with the correlated case, we present the overload probabilities in an array in Figure 3.13(a), where for each of the possible 435 pairs (i,j) of injection nodes, Π_{ij} is plotted in a color scale (see the scale bar in the figure). In the upper triangle of the array above its diagonal, the Π_{ij} are given for the uncorrelated case, and in the lower triangle for the correlated case.

The first result from the single node replacement, that the line overload probabilities vary strongly with the location, can be substantiated with variation in a range of 10^0 to 10^{-5} (see the scale of the color bar). Therefore, the embedding of the same average power with two wind farms can reach probabilities about two orders of magnitude smaller than the single node case, which demonstrates the possible advantage of decentralized wind power generation. Furthermore, one can see that certain nodes tend to have a low probability independent of the second node. These nodes are 4, 10, 16, 20 and 30, which also yield the lowest probability under the single node injection. The single node value seems to be a good indicator for the possible pair combinations. Furthermore, one can now clearly see the three mentioned vulnerable regions of the single node case. A combination of any of those nodes always results in the highest probabilities. The bad effect can be compensated for when paired with a good location, since both wind farm sizes are scaled according to the lowest probability scenario (see subsection 3.2.2). This scaling means that a pair consisting of a vulnerable node, for example 11, and a resilient node, such as 4, can result in a relatively low probability. In such a case, the scaling factor of the wind farm 4 is high compared to the factor at node 11 ($\lambda_4 \gg \lambda_{11}$). This common feature for the correlated and uncorrelated case, however, does not imply that the best pairs of injection nodes are the same for

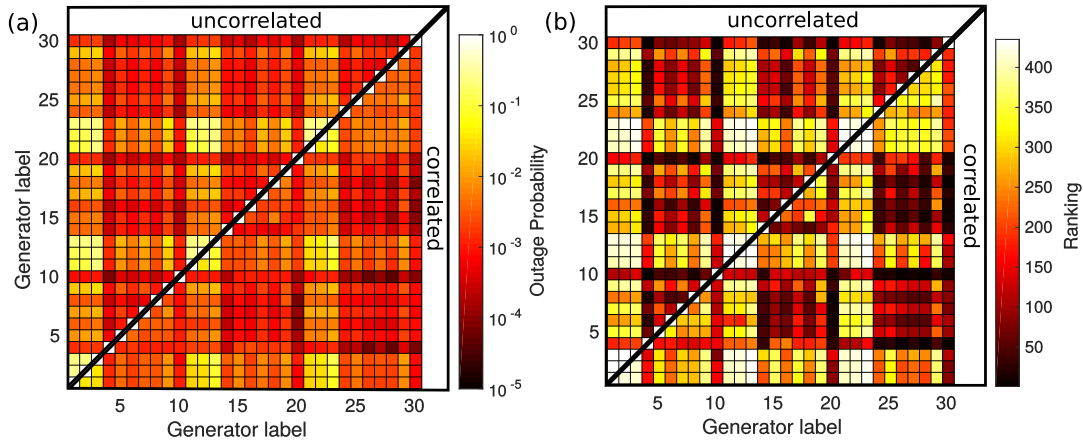


FIGURE 3.13: (a) Overload probability Π_{ij} of all 435 pairs in the uncorrelated case (upper triangle) and correlated case (lower triangle) for $g_{tot} = 200$ MW. (b) The ranking of the node pairs according to the overload probability for both correlation cases.

Uncorrelated	$\Pi_{ij} \times 10^{-5}$	Correlated	$\Pi_{ij} \times 10^{-5}$
4, 10	7.35	10, 28	4.35
4, 20	13.6	4, 28	5.31
10, 16	15.6	10, 26	5.97
10, 24	17.0	4, 26	6.82
20, 30	17.1	18, 30	8.27

TABLE 3.1: The five node pairs with the lowest overload probability for uncorrelated and correlated wind farm locations.

uncorrelated and correlated wind powers. The five pairs yielding the lowest Π_{ij} are listed in Table 3.1. While one of the nodes with numbers 4, 10, and 30 appears in all pairings for both the uncorrelated and correlated cases, its “pairing node” is always different, i.e. none of the five best pairs in the uncorrelated case agrees with one of the five best pairs in the correlated case. This result demonstrates the relevance of wind power correlations in the search for optimal wind feeding nodes. Pairs of the same rank in Table 3.1 have about two to three times lower overload probabilities for correlated wind powers. For completeness, we include in Figure 3.13(b) the ranking of all node pairs ordered by their overload probability, starting with zero for the lowest probability.

3.4 Outlook for the German power grid

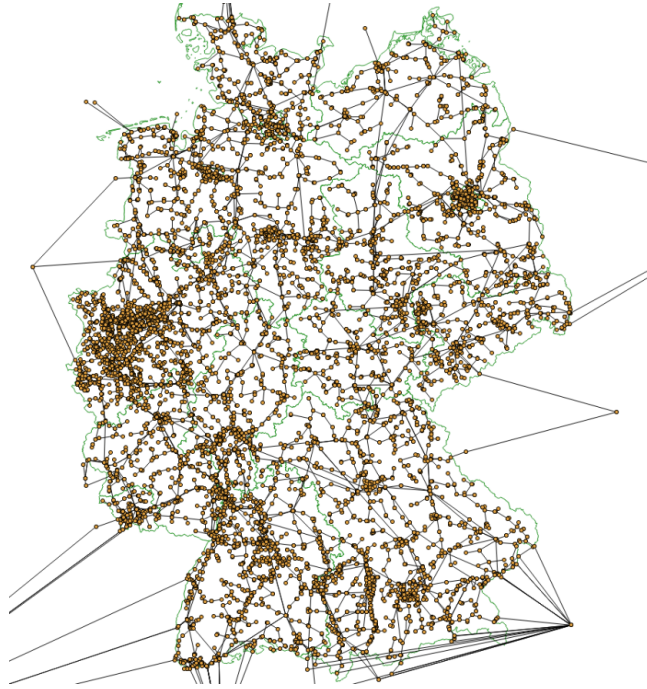


FIGURE 3.14: The *open_eGo* grid data with the voltage levels 110 kV, 220 kV and 380 kV consisting of 11309 buses with 3615 loads and 24366 generators, 19151 lines and 526 transformers. The buses are yellow circles and the transmission lines are illustrated as transparent gray lines.

In section 3.3 we investigated the resilience of a test grid against line overloads under fluctuating renewable power injection. The results demonstrate that the process of distinguishing the optimum position for new wind farms or finding dangerous regions in power grids depends on the topology and properties of the grid. The next step of this thesis would be to apply the established methods to the German power grid. However, there are multiple problems utilizing the methods on the German grid. First, the properties of the German power grid are not completely publicly available. This limitation can be solved by using one of the open source projects, that extract or extrapolate the data needed for power grid analysis (see section 2.4). In this thesis, the grid data from the *open_eGo* project will be used. The *open_eGo* power grid with over 11000 different buses and 19000 lines is provided in Figure 3.14 [43].

Secondly, there are thousands of renewable sources from individual turbines or solar systems to large parks. The established methodology treats the fluctuating resources as a variable in the power flow analysis. This high number would result in a high-dimensional space spanned by all fluctuating sources, which is difficult to solve by analytical or numerical means. Therefore we will apply a numerical Monte Carlo approach, where the renewable sources are replaced by a Weibull distributed random variable. The grid is still modeled through the linear power flow equation to determine the flow through each transmission line, meaning, that in every Monte Carlo step, for every renewable source a Weibull distributed variable is drawn. However, we do not encounter daily or even weekly overloads of transmission lines in our current power grid, and the optimal overload probabilities in section 3.3 substantiate the assumption, that overloads from renewable power only happen in rare instances. Therefore, if we apply a numerical Monte Carlo method, we will most likely not find any overloads without

a large sample number. The main idea is again to take a snapshot of the grid in a stable state where the timescale of wind fluctuation is short compared to fluctuation in demand, but long compared to the regulating reaction of the conventional generators. The following paragraphs will outline ideas on how to investigate the German grids stability under these conditions and address the following question: How will the difference between hourly snapshots and sub-hour fluctuation of renewable sources impact the German grid resilience against transmission line outages?

Since overloads are rare events, one interesting quantity is the utilization rate $u_{ij} = P_{ij}/P_{ij}^{\max}$ of a transmission line connecting nodes i and j . An overload would then correspond to $u_{ij} > 1$, but also allow dangerous lines close to 1 to be determined. For the first idea we will calculate u_{ij}^{hour} with the average wind power on the time scale of one hour. For this hour the generators and loads are in the already discussed quasi-static state. Then, in each Monte Carlo step k , the utilization rate u_{ij}^k is calculated through variation of every renewable source with a Weibull distributed value. This distribution should have the same average as the actual used value for u_{ij}^{hour} . Following these steps, it becomes possible to compare the hourly average value u_{ij}^{hour} with the average value of all N Monte Carlo steps $\langle u_{ij} \rangle = \frac{1}{N} \sum_k^N u_{ij}^k$. Therefore we begin with a set of N_{hour} hourly snapshots of the grid in a stable state of an OPF solution. Next, we calculate the difference $\Delta u_{ij} = u_{ij}^{\text{hour}} - \langle u_{ij} \rangle$ for each line in each hourly snapshot. In the histogram of Δu_{ij} all lines from all hourly snapshots will display the average influence of sub-hour fluctuations. Some further ideas include:

- Investigate the distribution of all u_{ij}^k , where the accordingly u_{ij}^{hour} is subtracted, to identify the rate of extreme events.
- Calculate the numerical overload probability P_{ij} at one hourly time step of one line with the integral from 1 to ∞ over all u_{ij}^k for this hour, then compare this probability with the corresponding u_{ij}^{hour} value in a scatter plot of all lines and hours.
- Derive the correlation of u_{ij}^k of a line and the distribution of renewable power in the neighborhood.
- Since wind turbines have a wind velocity cut-off, the influence of a truncated Weibull on the overload probability or rather on the utilization rate is of interest. One could also optimize for the cut-off value, that prevents $u_{ij} > 1$.
- Another interesting quantity would be the risk assessment $\frac{\gamma}{\gamma^h}$ of the scaling factor γ , where γ^h is the proportion of renewable power in the hourly OPF solution.

Chapter 4

Conclusion

With the percentage of renewable power production increasing, accompanied by a change in structure and components of the power grid, power flow dynamics can also be assumed to be changing.

In this thesis we investigated the overload probabilities of transmission lines in power grids under wind power injection. Specifically, we studied the resilience of the IEEE RTS-96 grid when one and two conventional generators are replaced by wind farms, and with a given total average wind power production. The method used to calculate the overload probabilities is based on the linear power flow equations, and a quasi-static grid response is assumed. For the wind speed distribution, we used the Weibull distribution with a typical shape parameter of $k = 2$. For the injection from two wind farms the limiting cases of uncorrelated and completely correlated wind speeds were compared. The probabilities for the two-node replacement were optimized by adjusting the scale parameters of the Weibull distribution according to the wind farm sizes. Furthermore, ideas to expand the method were presented to analyze the German transmission grid.

The study of the IEEE RTS-96 grid resulted in four main findings. First, the overload probability varies strongly with the location of the wind farm in the cases of both one and two replaced generators. Second, the decentralization of the same average wind power through two wind farms instead of one reduces the overload probability by two orders of magnitude. Third, the spatial correlation between the optimal locations of two wind farms differ between the uncorrelated and completely correlated by a factor of two or three. Finally, it is possible to gain insight into the coupling between two fluctuating sources in the power grid only from the feasibility region, which is defined by the topology and the quasi-static state of the grid; to reach this conclusion, we followed the methodology reported in [23].

The validity of the quasi-static approach, which assumes no change in demand on the time scale of wind power fluctuations, is an important issue in this work and should to be considered for future research. This problem is closely connected to the question whether, common rescaling of the conventional generators, as a response to wind power fluctuations, reflects the standard controlling mechanism and the time scales where these controls intervene. Since no data for real wind power injection with a high frequency of at least 1 Hz was available, the short time fluctuations of wind power could not be validated in this thesis. The conversion from wind speed to power is more complex than the cubic function and more accurately described by the power curve. The influence on the findings of the more accurate power curve with saturation and cut-off needs investigation. Furthermore, the overall assumption that wind speeds are described by the Weibull distribution is not clear for the short time scales, which are assumed to justify the quasi-static approach. In addition the stability

of the power grid is defined through line overload, but standard stability definitions are determined by frequency and voltage criteria. Including voltage and frequency is not easily possible, since the linear power flow model neglects these criteria. Although the linear description is widely used for modeling the transmission grid, one must keep in mind that in overload scenarios the grid is no longer in a typical state and the assumptions of the linearization may no longer be true. In addition, the reactive power flow is completely neglected; however, as long as the linearization is correct the reactive flow is constant.

Generally, the goal is to develop methods and tools to allow accurate and comprehensive planning for extending power grids. One aspect of network expansion is to estimate risks when embedding wind parks or other fluctuating renewable sources. This work is only one step towards this goal and will be extended in future research. Therefore, we started with the linear model that has already produced interesting results. The results for the IEEE RTS-96 grid can be further investigated by evaluating whether the strong variation in the overload probability comes from the grid's heterogeneity, a factor which is often neglected in research [14]. The impact of different average wind powers can also be examined further. It is important to clarify that exact predictions of the overload probability may not even be necessary when comparing different scenarios, as long as the relations are correct. To more accurately match the reality, the next research step is to use the real power grid data as presented in the outlook for the German grid. Moreover, this method could be used to calculate not only the overload probability, but also successive overloads. This calculation could be done by simply removing the overloaded line and reapplying the method. The probability of grid-wide blackouts, such as the blackout of November 2006, that are caused by wind fluctuations could then be estimated.

Appendix A

Supplementary material

A.1 Example of an resistive network calculation

The electric current equation in an resistive network can be summarized in a matrix multiplication. The following example will demonstrate this simplification. Figure A.1 illustrates a example network with three nodes. Each node pair is connected to through a transmission line with admittance y_{kl} from node k to l .

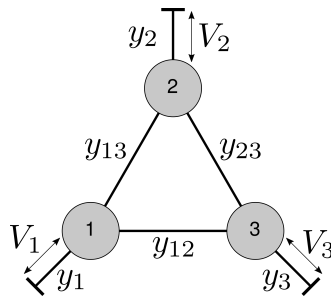


FIGURE A.1: Example resistive network with three nodes connected through admittances.

The current at node 1 consists of the two currents to nodes 2 and 3, and the current to the ground. Consequently, I_1 results as

$$I_1 = V_1 y_1 + (V_1 - V_2) y_{12} + (V_1 - V_3) y_{13}. \quad (\text{A.1})$$

This equation can be reorganized to

$$I_1 = V_1 (y_1 + y_{12} + y_{13}) + V_2 (-y_{12}) + V_3 (-y_{13}), \quad (\text{A.2})$$

and written down for the other nodes

$$I_2 = V_2 (y_2 + y_{12} + y_{23}) + V_1 (-y_{12}) + V_3 (-y_{23}) \quad (\text{A.3})$$

$$I_3 = V_3 (y_3 + y_{13} + y_{23}) + V_1 (-y_{13}) + V_2 (-y_{23}). \quad (\text{A.4})$$

It is assumed that $y_{kl} = y_{lk}$. Equation A.3 can be written as a matrix equation in the form of

$$\begin{bmatrix} I_1 \\ I_2 \\ I_3 \end{bmatrix} = \begin{bmatrix} y_1 + y_{12} + y_{13} & -y_{12} & -y_{13} \\ y_2 + y_{12} + y_{23} & -y_{12} & -y_{23} \\ y_3 + y_{13} + y_{23} & -y_{13} & -y_{23} \end{bmatrix} \begin{bmatrix} V_1 \\ V_2 \\ V_3 \end{bmatrix}. \quad (\text{A.5})$$

This matrix equation pattern can be extended for any number of nodes n

$$I_k = V_k \left(y_k + \sum_{l=1, l \neq k}^n y_{kl} \right) + \sum_{l=1, l \neq k}^n V_l (-y_{kl}). \quad (\text{A.6})$$

Next, this equation can be summarized as

$$I_k = \sum_{l=1}^n y_{kl} V_l, \quad (\text{A.7})$$

with $y_{kk} = y_k$. Finally, the equation can be written in a matrix equation $\mathbf{I} = \mathbf{YV}$ where \mathbf{Y} is the admittance matrix, with elements y_{kl} .

A.2 Example calculation of the linear power flow equations

This section illustrates the calculation process of the linear power flow equation by solving a simple example consisting of four nodes without any shunt elements (see Figure A.2).

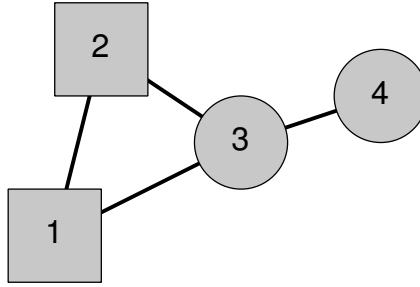


FIGURE A.2: Example network consisting of two generators (squares) and two loads (circles) as well as transmission lines.

Assumed that the susceptance matrix B and the electric power vector P at each node is known, it becomes possible to calculate the voltage phases vector θ through the linear power flow equation Equation 2.24a

$$P = \begin{bmatrix} 3 \\ 1 \\ -2 \\ -2 \end{bmatrix} = \begin{bmatrix} 20 & -10 & -10 & 0 \\ -10 & 20 & -10 & 0 \\ -10 & -10 & 30 & -10 \\ 0 & 0 & -10 & 10 \end{bmatrix} \begin{bmatrix} \theta_1 \\ \theta_2 \\ \theta_3 \\ \theta_4 \end{bmatrix} = B\theta. \quad (\text{A.8})$$

All values are chosen arbitrarily and units are ignored. Because the matrix B is singular, this linear system of equations can not be uniquely solved. This overdeterminacy represents the physical property that only the phase differences are important. Therefore, one reference point with phase zero can be freely chosen. For this example, node two is chosen as reference point ($\theta_2 = 0$) and removed from the corresponding row and column of the equation system. This reduction leads to the system

$$\tilde{P} = \begin{bmatrix} 3 \\ -2 \\ -2 \end{bmatrix} = \begin{bmatrix} 20 & -10 & 0 \\ -10 & 30 & -10 \\ 0 & -10 & 10 \end{bmatrix} \begin{bmatrix} \theta_1 \\ \theta_3 \\ \theta_4 \end{bmatrix} = \tilde{B}\tilde{\theta}. \quad (\text{A.9})$$

The matrix \tilde{B} is invertible and the equation system can be solved with standard techniques, to obtain

$$\tilde{\theta} = \tilde{B}^{-1}\tilde{P} = \begin{bmatrix} 20 & -10 & 0 \\ -10 & 30 & -10 \\ 0 & -10 & 10 \end{bmatrix}^{-1} \begin{bmatrix} 3 \\ -2 \\ -2 \end{bmatrix} = \begin{bmatrix} 0.0\bar{6} \\ -0.1\bar{6} \\ -0.3\bar{6} \end{bmatrix}. \quad (\text{A.10})$$

Next, the reference node 2 must be reinserted

$$\theta = \begin{bmatrix} \theta_1 \\ \theta_2 \\ \theta_3 \\ \theta_4 \end{bmatrix} = \begin{bmatrix} 0.0\bar{6} \\ 0 \\ -0.1\bar{6} \\ -0.3\bar{6} \end{bmatrix}. \quad (\text{A.11})$$

A.3 Polygon example calculation

This section calculates the feasibility polygon area (see subsection 3.2.1) of an example grid. Therefore, the example grid provided in Figure A.3 will be investigated. The grid contains eight lines, two generators (nodes 1 and 2), two loads (nodes 3 and 4), and two wind farms (nodes 5 and 6) with production $g_1 \geq 0$ and $g_2 \geq 0$. For simplicity every node has only one bus type.

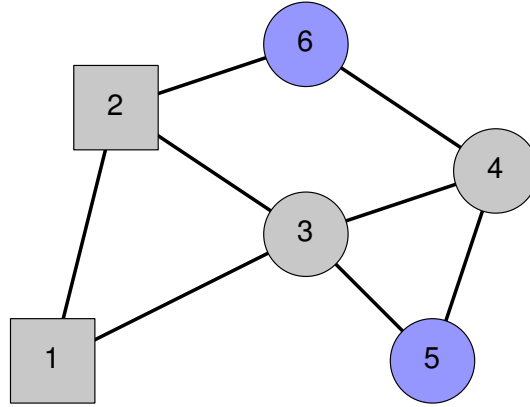


FIGURE A.3: Example power grid with two generators (grey squares), two loads (grey circles) and two wind farms (blue circles) connected by transmission lines.

The system is described through the voltage angles θ , calculated from the arbitrary chosen power vector P and susceptance matrix B

$$\theta = B^{-1}P = \begin{bmatrix} 40 & -20 & -20 & 0 & 0 & 0 \\ -20 & 60 & -20 & 0 & 0 & -20 \\ -20 & -20 & 80 & -20 & -20 & 0 \\ 0 & 0 & -20 & 60 & -20 & -20 \\ 0 & 0 & -20 & -20 & 40 & 0 \\ 0 & -20 & 0 & -20 & 0 & 40 \end{bmatrix}^{-1} \begin{bmatrix} \gamma 3 \\ \gamma 5 \\ -4 \\ -4 \\ g_1 \\ g_2 \end{bmatrix}, \quad (\text{A.12})$$

with γ the common factor of the generators as reaction to the renewable power to balance net power with

$$\gamma = \frac{(P_3^d + P_4^d) - (g_1 + g_2)}{(P_1^g + P_2^g)} = 1 - \frac{g_1}{8} - \frac{g_2}{8}. \quad (\text{A.13})$$

For zero wind production ($g_1 = g_2 = 0$) the grid is balanced with $\gamma = 1$. If $\gamma = 0$, the whole production originates from the wind farms. Because of the coefficient *gamma* in P , every generator is a linear function of g_i . Next, the coefficients α and β from Equation 3.5 are calculated and expressed through the matrix

$$\theta = \alpha + \beta \begin{bmatrix} g_1 \\ g_2 \end{bmatrix} \approx \begin{bmatrix} 0 \\ -0.0017 \\ -0.1483 \\ -0.2117 \\ -0.1800 \\ -0.1067 \end{bmatrix} + \begin{bmatrix} 0 & 0 \\ 0.0002 & 0.0069 \\ 0.0185 & 0.0119 \\ 0.0265 & 0.0231 \\ 0.0475 & 0.0175 \\ 0.0133 & 0.0400 \end{bmatrix} \begin{bmatrix} g_1 \\ g_2 \end{bmatrix}. \quad (\text{A.14})$$

The limiting planes from Equation 3.7 can be calculated with the coefficients. The feasibility region is also limited by the factor γ , because $\gamma > 1$ indicated power excess in the grid. Consequently, the polygon is limited by two planes for every connection line and one plane from $\gamma_0 = 1$, which results in 17 planes in the g_1 - g_2 space. The planes and feasibility region is illustrated in Figure A.4.

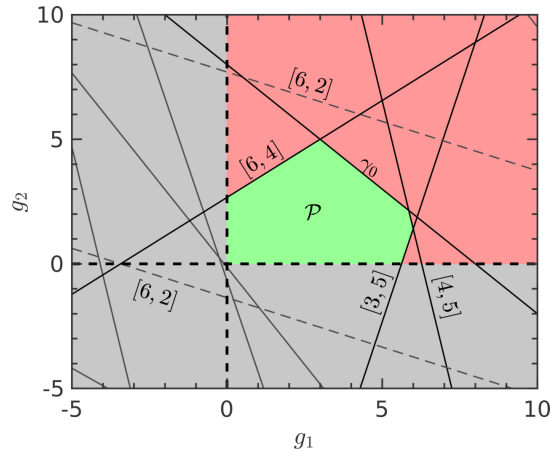


FIGURE A.4: The feasible area \mathcal{P} of the grid from Figure A.3 (green polygon) and the infeasible region (red) as well as the line constraints and γ_0 condition.

Every line in Figure A.4 corresponds to one connection line or γ_0 . For example, the dashed line in the upper half of the figure represents the line conditions connection node 6 and 2. The second limiting condition from line [6,2] is also marked as a dashed line in the lower half of the figure, but is not relevant, because it is in the negative region of wind power. The green polygon is the feasible area \mathcal{P} of the grid, limited through the four edges [6,4], γ_0 , [4,5] and [3,5]. If one of these lines is crossed, the corresponding condition is broken and the system is no longer feasible. All other line conditions are outside of the polygon and thus irrelevant. The form and number of limiting edges varies with the investigated grid, and the condition γ_0 is not always relevant.

A.4 Change of variable - Weibull

x is a continuous random variable with the Weibull probability density function

$$f(x; \lambda, k) = \begin{cases} \frac{k}{\lambda} \left(\frac{x}{\lambda}\right)^{k-1} e^{-(x/\lambda)^k} & x \geq 0, \\ 0 & x < 0. \end{cases} \quad (\text{A.15})$$

If $y(x) = x^3$, the probability density function $g(y)$ can be calculated with the change of variable theorem for $x \geq 0$

$$g(y) = \frac{f(x; \lambda, k)}{|y'(x)|} = \frac{\frac{k}{\lambda} \left(\frac{x}{\lambda}\right)^{k-1} e^{-(x/\lambda)^k}}{3x^2} \quad (\text{A.16})$$

$$= \frac{\frac{k}{\lambda} \left(\frac{y^{1/3}}{\lambda}\right)^{k-1} e^{-(y^{1/3}/\lambda)^k}}{3y^{2/3}} \quad (\text{A.17})$$

$$= \left(\frac{k}{\lambda}\right) y^{-\frac{2}{3}} y^{\frac{k}{3}-\frac{1}{3}} \left(\frac{1}{\lambda^3}\right)^{\frac{k}{3}-\frac{1}{3}} e^{-(y^{1/3}/\lambda)^k}. \quad (\text{A.18})$$

Next, the equation is expanded with $\frac{\lambda^2}{\lambda^2}$ (note $\lambda^2 = \left(\frac{1}{3}\right)^{-\frac{2}{3}}$)

$$g(x) = \frac{k}{\lambda^3} \left(\frac{x}{\lambda^3}\right)^{\frac{k}{3}-1} e^{-(x/\lambda^3)^{\frac{k}{3}}} \quad (\text{A.19})$$

and replacing the coefficients k and λ by

$$\tilde{k} = \frac{k}{3} \quad (\text{A.20})$$

$$\tilde{\lambda} = \lambda^3 \quad (\text{A.21})$$

the Weibull function

$$g(y; \tilde{\lambda}, \tilde{k}) = f(x^3; \lambda^3, \frac{k}{3}) = \begin{cases} \frac{\tilde{k}}{\tilde{\lambda}} \left(\frac{y}{\tilde{\lambda}}\right)^{\tilde{k}-1} e^{-(y/\tilde{\lambda})^{\tilde{k}}} & y \geq 0, \\ 0 & y < 0 \end{cases} \quad (\text{A.22})$$

is obtained. Consequently, the transformation of $y = x^3$ can be expressed by only transforming the Weibull shape and scale parameter through Equation A.20 and Equation A.21.

A.5 Numerical method of solving the double integral and optimization

Section 3.2.2 includes the problem of solving a double integral over the area A of a convex polygon \mathcal{P} . This section presents the procedure and numerical methods used to solve this problem and includes an example. For a tidy solution, the underlying physics of wind generation will be neglected. Finally, in the last part of this section, the optimization method of subsection 3.2.2 will be illustrated.

The integral problem is defined as followed. The two integrals

$$I_1 = \int_0^\infty dx \int_0^\infty dy f(x,y) \mathcal{W}_1(x) \mathcal{W}_2(y) \tag{A.23}$$

$$I_2 = \int_0^\infty dx \int_0^\infty dy f(x,y) \mathcal{W}_1(x) \mathcal{W}_2(x)(x+y) \tag{A.24}$$

have to be solved. The solution

$$\int_0^a dx \mathcal{W}_i(x) = C_i(a) \tag{A.25}$$

is known, with $f(x,y) = 1$ if $(x,y) \in \mathcal{P}$ and otherwise zero.

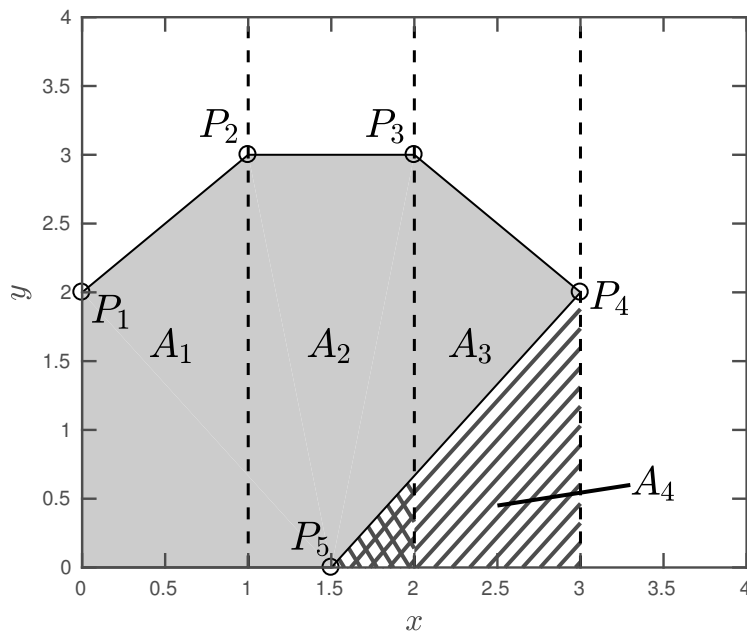


FIGURE A.5: The polygon \mathcal{P} with area A defined through the points P_1 - P_5 and both axes (gray). The area A is divided into four different integration areas. Area A_2 includes the cross shaded part, A_3 includes the single shaded part and area A_4 consists of both shaded areas.

Figure A.5 illustrates an example polygon defined through five points P_1 - P_5 and both axes. Each point P_i has the coordinates x_i and y_i . $f(x,y)$ defines the indicator function of the gray area in Figure A.5. If the straight line equation h_{ij} between point

P_i and P_j is known, it becomes possible to divide I_1 into the four areas A_1 - A_4

$$I_1 = I_{1,1} + I_{1,2} + I_3 + I_4 \quad (\text{A.26})$$

$$I_{1,1} = \int_{x_1}^{x_2} dx \int_0^{h_{12}} \mathcal{W}_1(x)\mathcal{W}_2(y) \quad (\text{A.27})$$

$$I_{1,2} = \int_{x_2}^{x_3} dx \int_0^{h_{23}} \mathcal{W}_1(x)\mathcal{W}_2(y) \quad (\text{A.28})$$

$$I_{1,3} = \int_{x_3}^{x_4} dx \int_0^{h_{34}} \mathcal{W}_1(x)\mathcal{W}_2(y) \quad (\text{A.29})$$

$$I_{1,4} = \int_{x_4}^{x_5} dx \int_0^{h_{45}} \mathcal{W}_1(x)\mathcal{W}_2(y). \quad (\text{A.30})$$

The last area A_4 is negative, because $x_4 > x_5$. The simplification of starting the integral from zero, despite the fact that the polygon boundaries do not match the y-axes, only becomes possible, because the last area A_4 subtracts the falsely added areas (cross shaded for A_2 and single shaded for A_3). This simplification is always possible since the polygon is convex.

With Equation A.25 the integral $I_{1,1}$ (analogous for $I_{1,2}$ - $I_{1,4}$) becomes

$$I_{1,1} = \int_{x_1}^{x_2} dx \mathcal{W}_1(x)\mathcal{C}(h_{12}), \quad (\text{A.31})$$

which is numerically solvable with the *MATLAB* [56] function *integral()*.

The integral I_2 is analogically divided into four areas, with the resulting integral

$$I_{2,1} = \int_{x_1}^{x_2} dx \int_0^{h_{12}} \mathcal{W}_1(x)\mathcal{W}_2(y)(x+y) \quad (\text{A.32})$$

and analogous for $I_{2,2}$ - $I_{2,4}$. This integral has to be solved with the *MATLAB* function *integral2()*. In doing so one encounters a problem with the first area A_1 , because *integral2()* has technical difficulties with the double singularity at (0,0) of the function $\mathcal{W}_1(x)\mathcal{W}_2(y)$. This problem is avoided by treating area A_1 differently than the others and divide it once more into three parts A_1^1 - A_1^3 as illustrated in Figure A.6. The first area A_1^1 is a square with arbitrary edge length ϵ starting at coordinate origin.

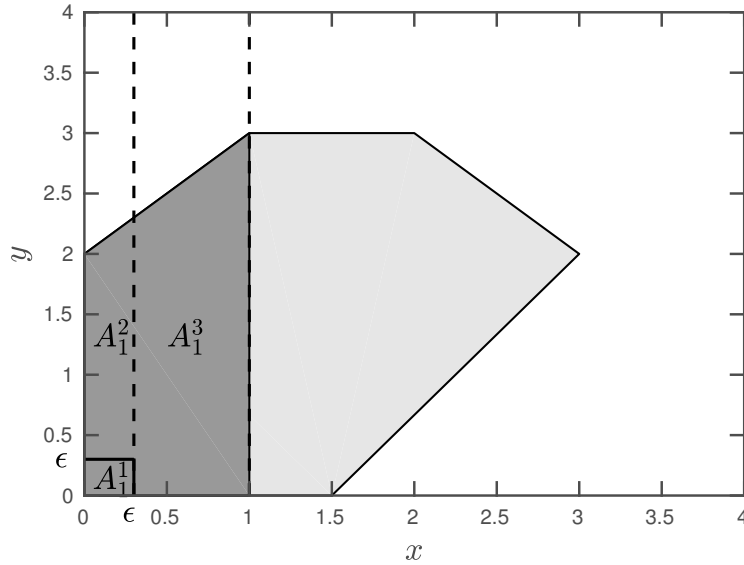


FIGURE A.6: The polygon \mathcal{P} from Figure A.5, with A_1 (darker area) additionally divided into the three areas A_1^1 - A_1^3 . Square A_1^1 is defined through the edge length ϵ .

The areas A_1^2 and A_1^3 can be solved with the `integral2()` function. For A_1^1 , which includes the problematic double singularity, the integral I_ϵ is

$$I_\epsilon = \int_0^\epsilon dx \int_0^\epsilon dy \mathcal{W}_1(x) \mathcal{W}_2(y) (x + y) \quad (\text{A.33})$$

$$= \mathcal{C}_2(\epsilon) \int_0^\epsilon dx \mathcal{W}_1(x) x + \mathcal{C}_1(\epsilon) \int_0^\epsilon dy \mathcal{W}_2(y) y. \quad (\text{A.34})$$

This equation is again solvable with `integral()`.

Next, to solve the optimization of λ_1 and λ_2 (see subsection 3.2.2) the MATLAB function `fmincon()`¹ is used. The following MATLAB code piece illustrates the implemented method. The letter l is easily mistaken as a 1.

```

1 % 200 MW average production
2 Pconst = 2;
3
4 % Define the function to minimize, here the overload
   probability for two nodes. The function variable is the
   lambda vector l with lambda_1 l(1) and lambda_2 l(2) as
   well as the polygon points coordinates x and y
5 fun = @(l) 1 - probTwo(l(1), l(2), x, y);
6
7 % Starting point
8 x0 = [1, 1];
9
10 % No linear conditions
11 A = [];
12 b = [];
13 Aeq = [];
14 beq = [];

```

¹<https://de.mathworks.com/help/optim/ug/fmincon.html>

```
15
16 % Nonlinear conditions
17 % Define the constraint function , here the total average of
    Pconst
18 ceq = @(l) -Pconst + doubleint(l(1),l(2),x,y);
19 c = []
20 noncond = [c ceq];
21
22 % Lower boundaries not zero , because of the double
    singularity , else fmincon may encounter problems
23 lb = [0.01 0.01];
24 % no upper boundary
25 ub = [];
26
27 % Run fmincon to minimize fun according to the set
    constraints
28 [x,fval,exitflag,output] = fmincon(fun, x0,A,b,Aeq,beq,lb,ub,
    noncond);
```

The functions *probTwo()* and *doubleint()* implement the solving methods presented above.

A.6 IEEE RTS-96 data tables

This section will present how the data needed for the linear power flow was extracted from the available tables. The IEEE RTS-96 was published in [55], but we used the data tables from https://www2.ee.washington.edu/research/pstca/rts/pg_tcart.htm. Table A.1 lists the relevant information for this thesis and from which table of the IEEE RTS-96 data set this information was taken.

Information	Source location
Power demand $P_j^{(d)}$	Table 1, column 4
Power generation $P_j^{(g)}$	Table 7, column 4
Lines $[jk]$	Table 12, columns 2 and 3
Reactances $x_{jk} = b_{jk}^{-1}$	Table 12, column 9
Rating $P_{[jk]}^{\max}$	Table 12, column 13

TABLE A.1: Information extracted from the IEEE RTS-96 test grid.

The corresponding tables are illustrated in Figure A.7. All generators were numbered according to their order in Table 1 from 1 to 30.

Table 1 - IEEE RTS-96 Bus Data (3 Areas)										Table 7 - Data of Generators at Each Bus							
BUS #	BUS NAME	BUS TYPE	MW LOAD	MVAR LOAD	GL	BL	Sub Area	Base kV	Zone #	Bus ID	Unit Type	ID #	PG MW	QG MVAR	Qmax MVAR	Qmin MVAR	VS pu
101	Abel	2	108	22	0	0	11	138	11	101	U20	1	10	0	10	0	1.035
102	Adams	2	97	20	0	0	11	138	12	101	U20	2	10	0	10	0	1.035
103	Adler	1	180	37	0	0	11	138	11	101	U76	3	76	14.1	30	-25	1.035
104	Agricola	1	74	15	0	0	11	138	11	101	U76	4	76	14.1	30	-25	1.035
105	Aiken	1	71	14	0	0	11	138	11	102	U20	1	10	0	10	0	1.035
106	Alber	1	136	28	0	1.00	11	138	12	102	U20	2	10	0	10	0	1.035
107	Alder	2	125	25	0	0	11	138	12	102	U76	3	76	7.0	30	-25	1.035
108	Alger	1	171	35	0	0	11	138	12	102	U76	4	76	7.0	30	-25	1.035
109	Ali	1	175	36	0	0	11	138	13	107	U100	1	80	17.2	60	0	1.025
110	Allen	1	195	40	0	0	11	138	13	107	U100	2	80	17.2	60	0	1.025
111	Anna	1	0	0	0	0	11	230	13	107	U100	3	80	17.2	60	0	1.025
112	Archer	1	0	0	0	0	11	230	13	107	U100	3	80	17.2	60	0	1.025

Table 12 - Branch Data													
ID#	From Bus	To Bus	L - miles	Perm. Lam-p	Dur	Tran. Lam-t	R pu	X pu	B pu	Con MVA	LTE MVA	STE MVA	Tr pu
A1	101	102	3	.24	16	0.0	0.003	0.014	0.461	175	193	200	0
A2	101	103	55	.51	10	2.9	0.055	0.211	0.057	175	208	220	0
A3	101	105	22	.33	10	1.2	0.022	0.085	0.023	175	208	220	0
A4	102	104	33	.39	10	1.7	0.033	0.127	0.034	175	208	220	0

ID# = Branch identifier.
 Inter area branches are indicated by double letter ID.
 Circuits on a common tower have hyphenated ID#.
 Lam-p = Permanent Outage Rate (outages/year).
 Dur = Permanent Outage Duration (Hours).
 Lam-t = Transient Outage Rate (outages/year).
 Con = Continuous rating.
 LTE = Long-time emergency rating (24 hour).
 STE = Short-time emergency rating (15 minute).
 Tr = Transformer off-nominal ratio.
 Transformer branches are indicated by Tr <> 0.

FIGURE A.7: Sections of the table 1,7, and 12 of the IEEE RTS-96 data set.

A.7 Overload probability correlation to topology (unweighted)

Figure A.8 presents the unweighted version of Figure 3.9 in subsection 3.3.1.

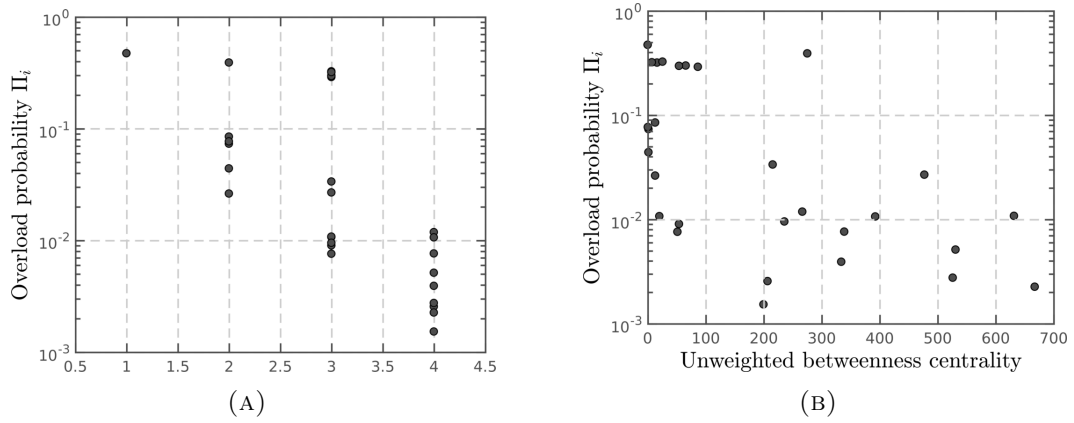


FIGURE A.8: The overload probability Π_i for single node i replacement with the corresponding unweighted node degree (left) and the unweighted betweenness centrality (right). Note that both plots are shown in a double logarithmic scale and the degree is in units of 100 MW.

A.8 QGis and GraphViz for illustrating grids

In this thesis the two free and open source softwares QGis [57] and GraphViz [58] were utilized to illustrate the networks. Graphviz has an extensive manual and will not be discussed in detail. For displaying the IEEE RTS-96 grid, the GraphViz algorithm *neato* was used. Some node position were manually adjusted to prevent unnecessary line overlapping.

QGis is geographic information system that supports viewing, editing, and analysis of geographic data. It also integrates plugins written in Python. For the two figures including the German power grid, a shapefile of the German grid and the plugin *Points2One* were used. The plugin can be found in the integrated plugin manager. For displaying the network nodes and edges, simply save the nodes as a CSV-file and use the *Add Delimited Text Layer* to read in x and y coordinates. For the edges, read in a CSV-file with the following format:

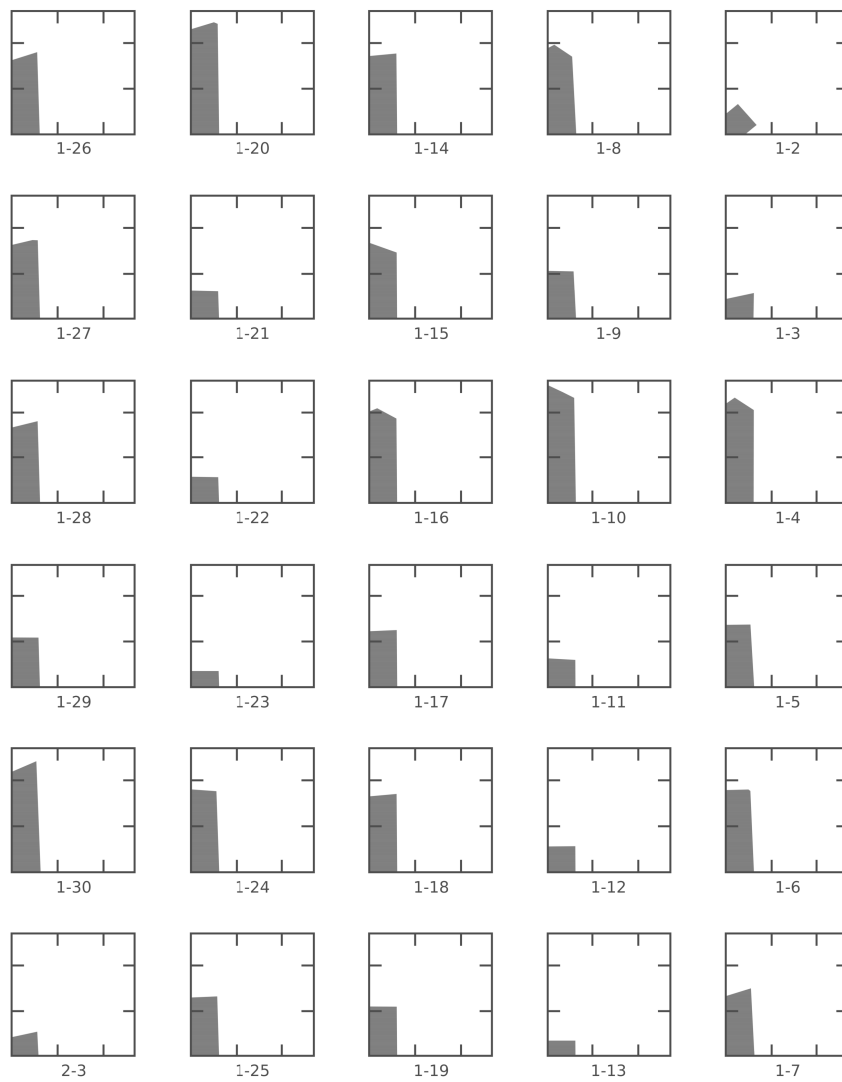
line id	order of points	x	y
edge 1	1	x_{start}^1	y_{start}^1
edge 1	2	x_{end}^1	y_{end}^1
edge 2	1	x_{start}^2	y_{start}^2
edge 2	2	x_{end}^2	y_{end}^2

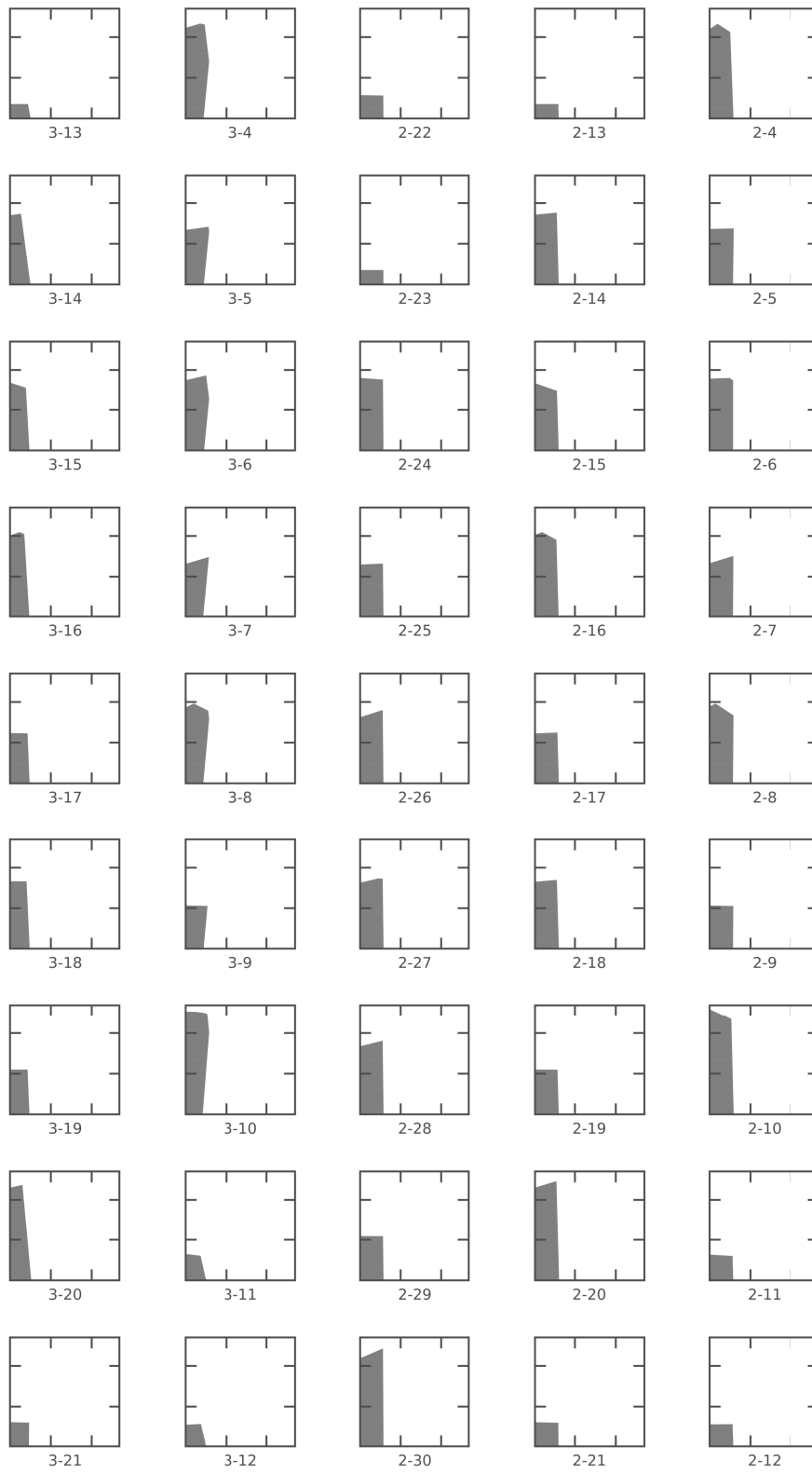
x_{start}^1 refers to the x coordinate of the start point of *edge 1* and x_{end}^1 to the coordinates of the end point. For every edge, this format results in two rows to define the position of the start and end position. In the *Points2One* plugin choose the *grouped by* option and select *line id* as value. For the *sorted by* option, select *order of points*. This should results in lines connecting every corresponding pair of nodes.

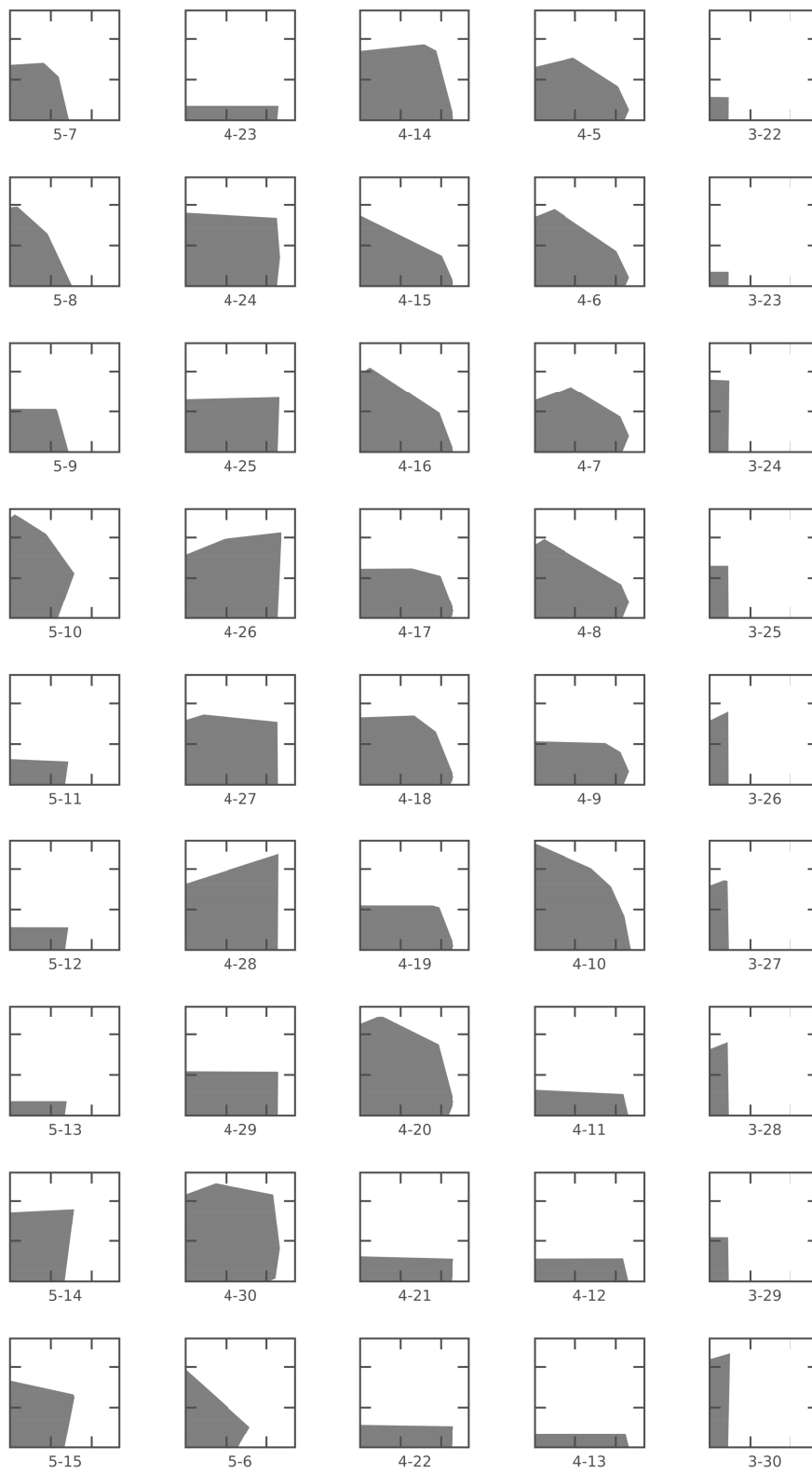
Appendix B

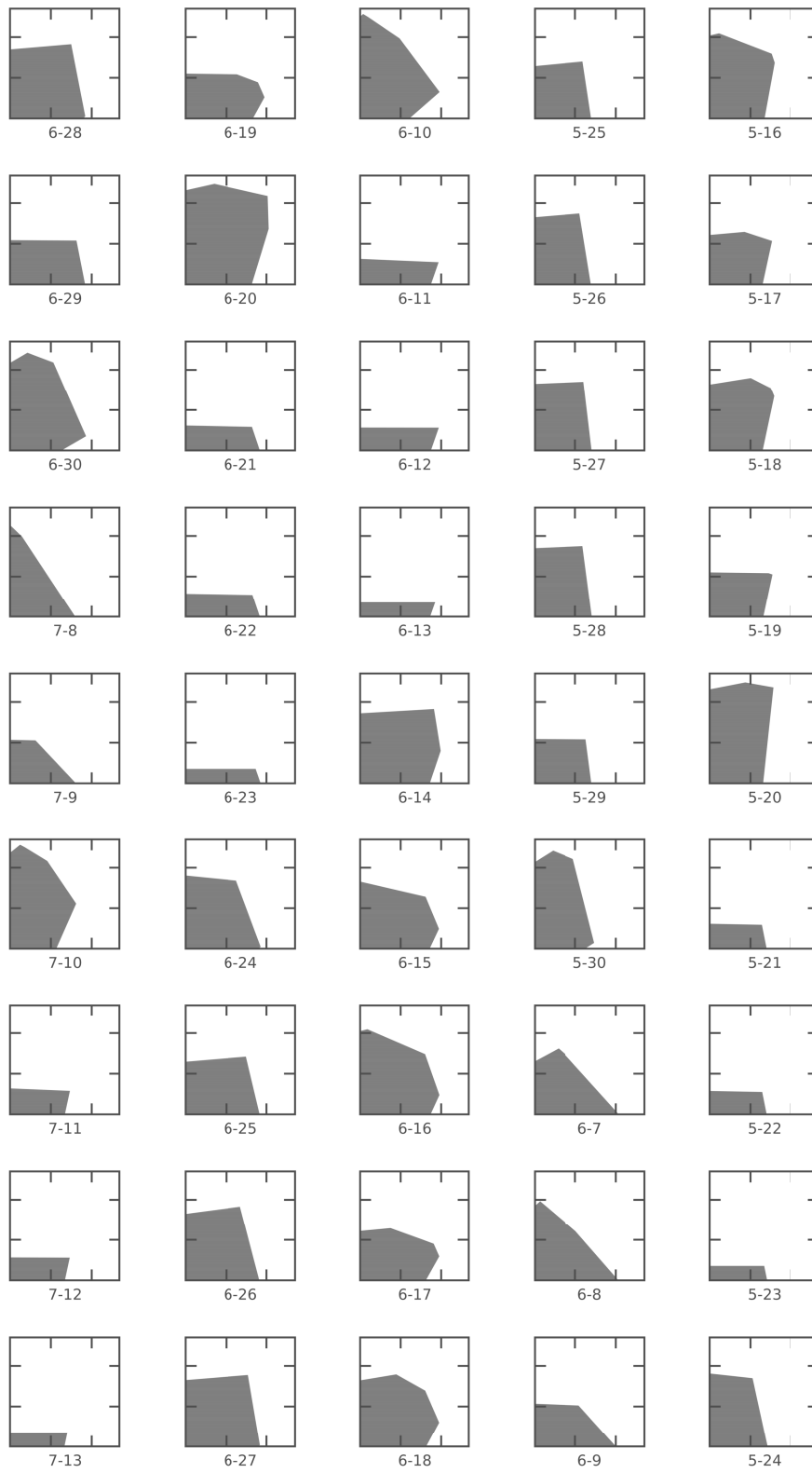
Polygons of the IEEE test grid

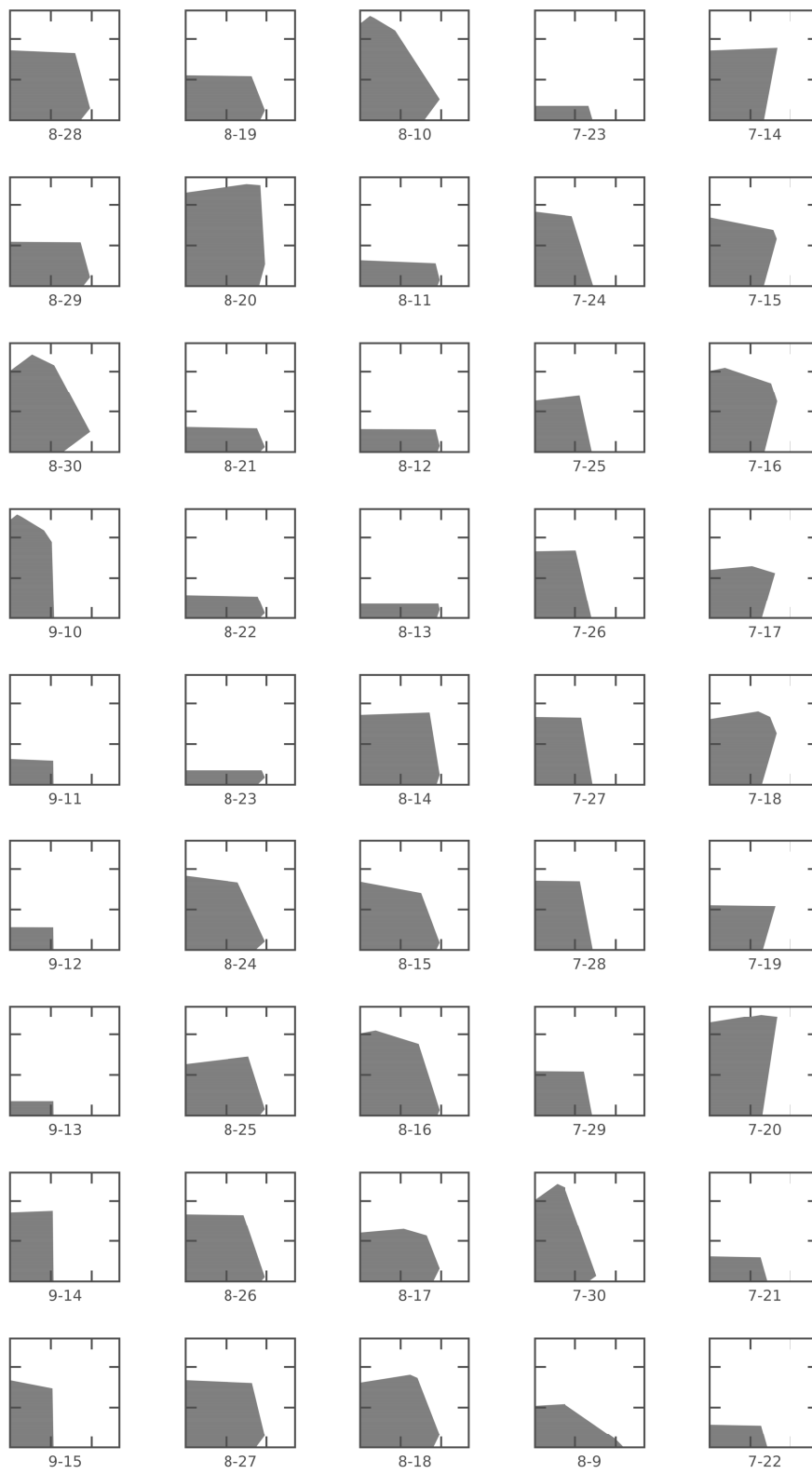
The following polygons illustrate the feasibility regions of the IEEE RTS-96 test grid (see subsection 3.3.2). The 30 generators result in overall 435 possible combinations. All axes range from 0 to 27 in units of 100 MW and the label $i - j$ corresponds to the replaced generator locations i and j .

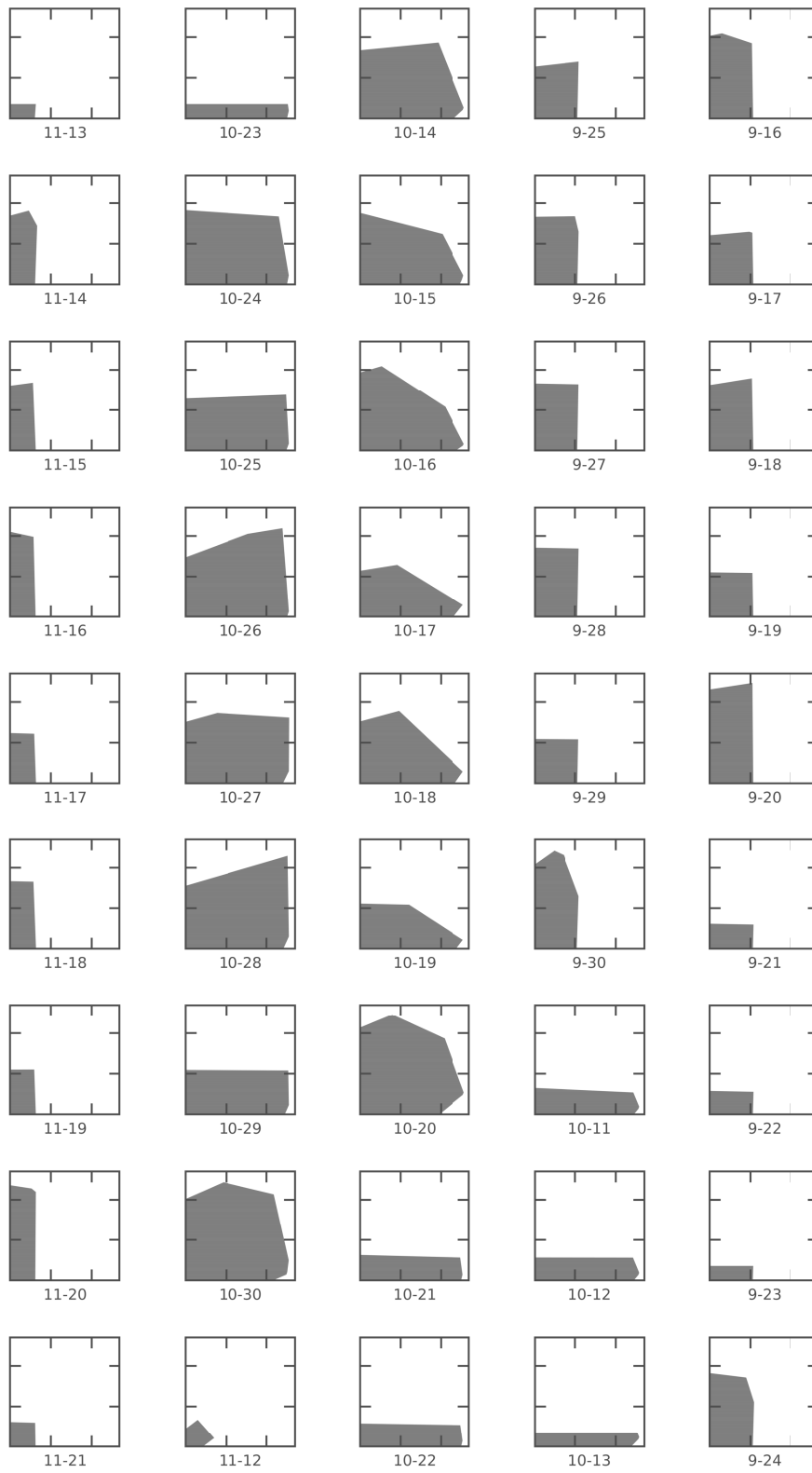


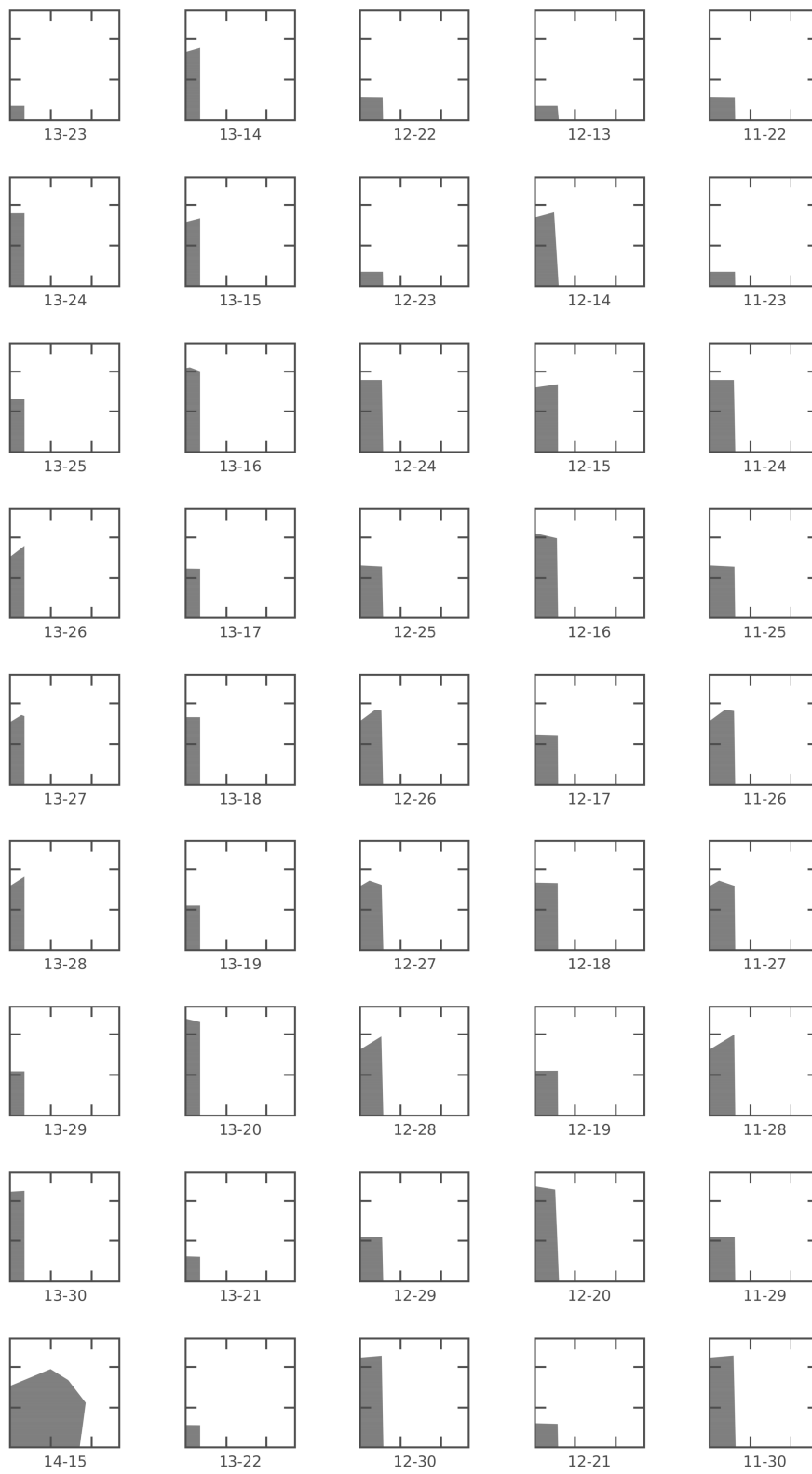


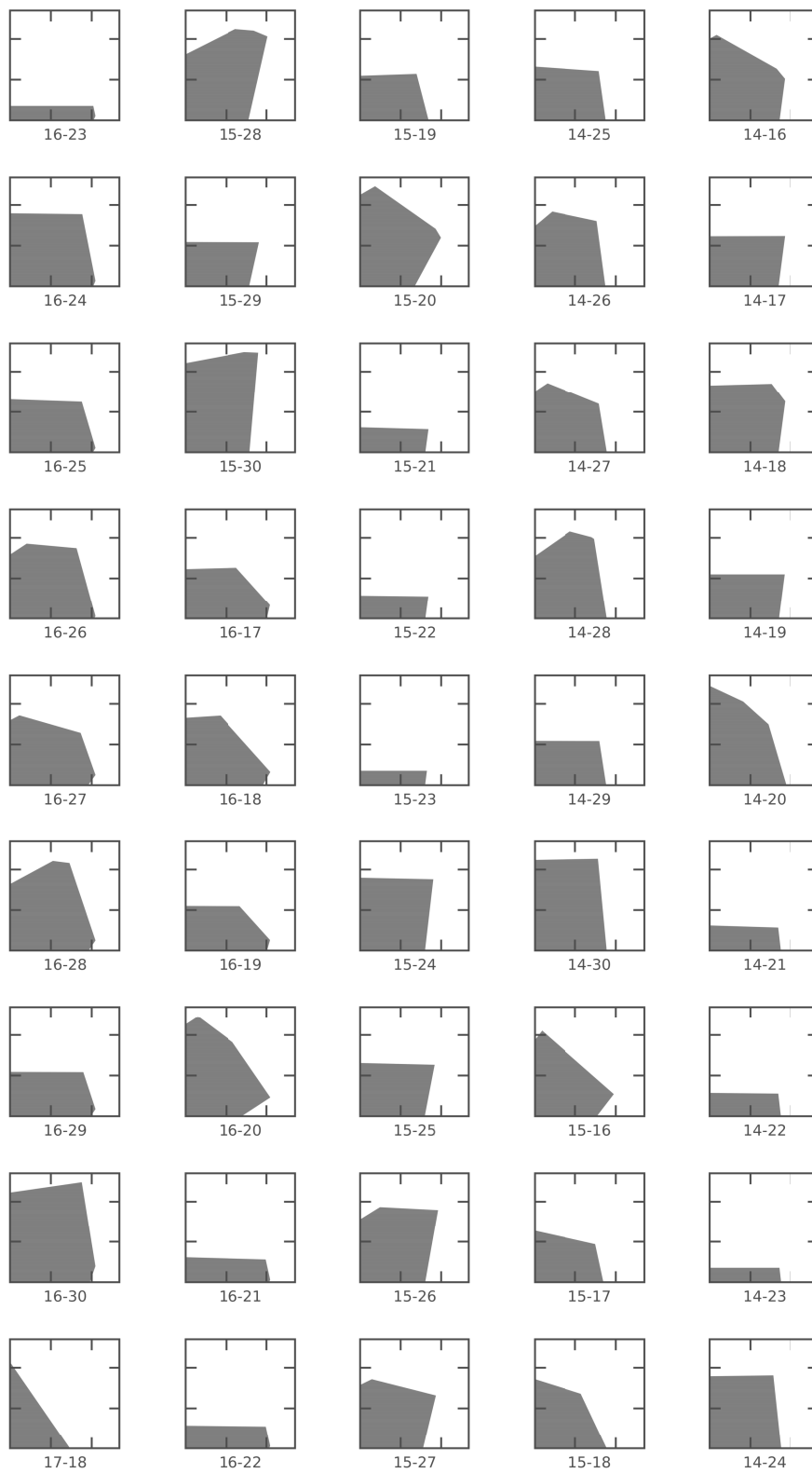


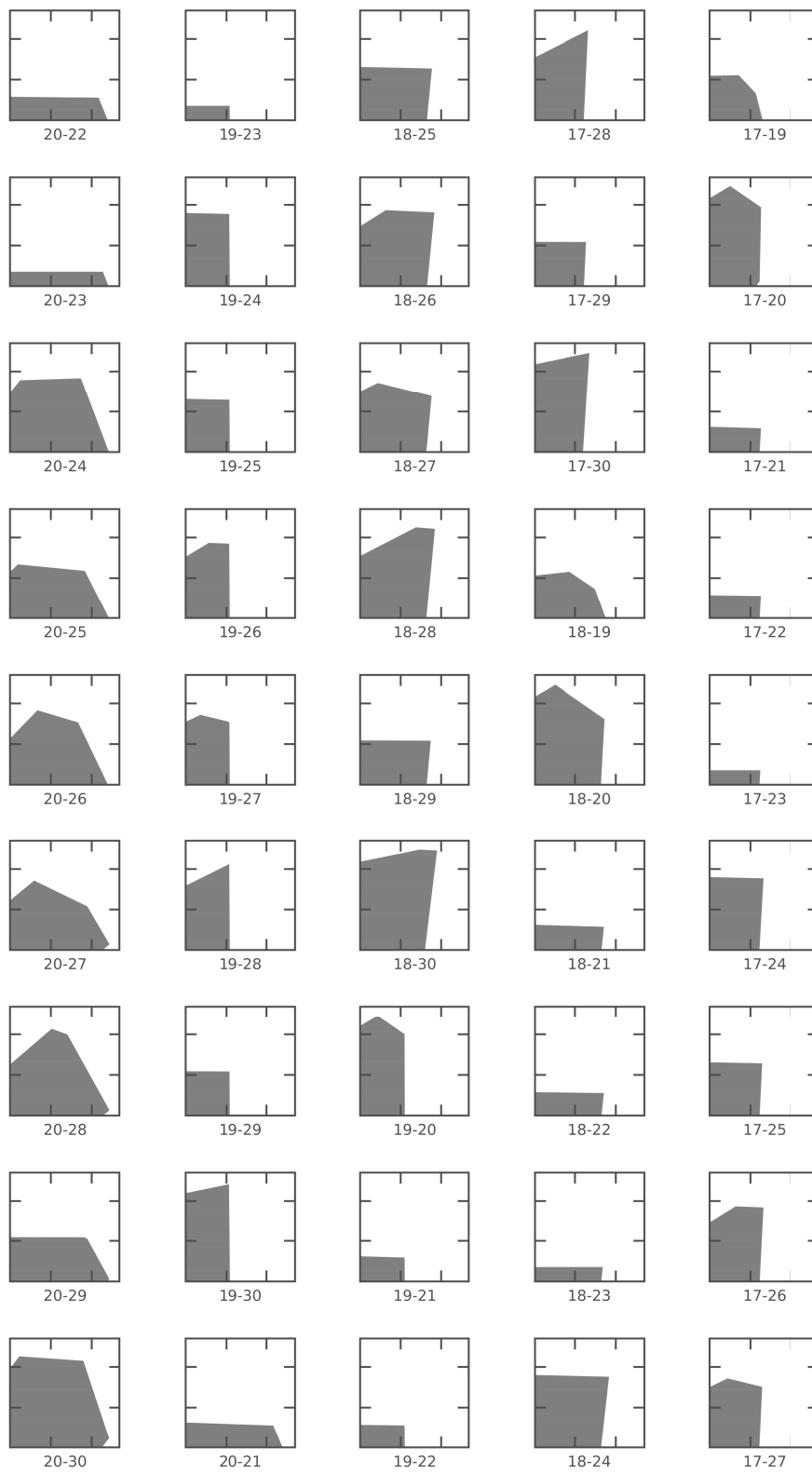


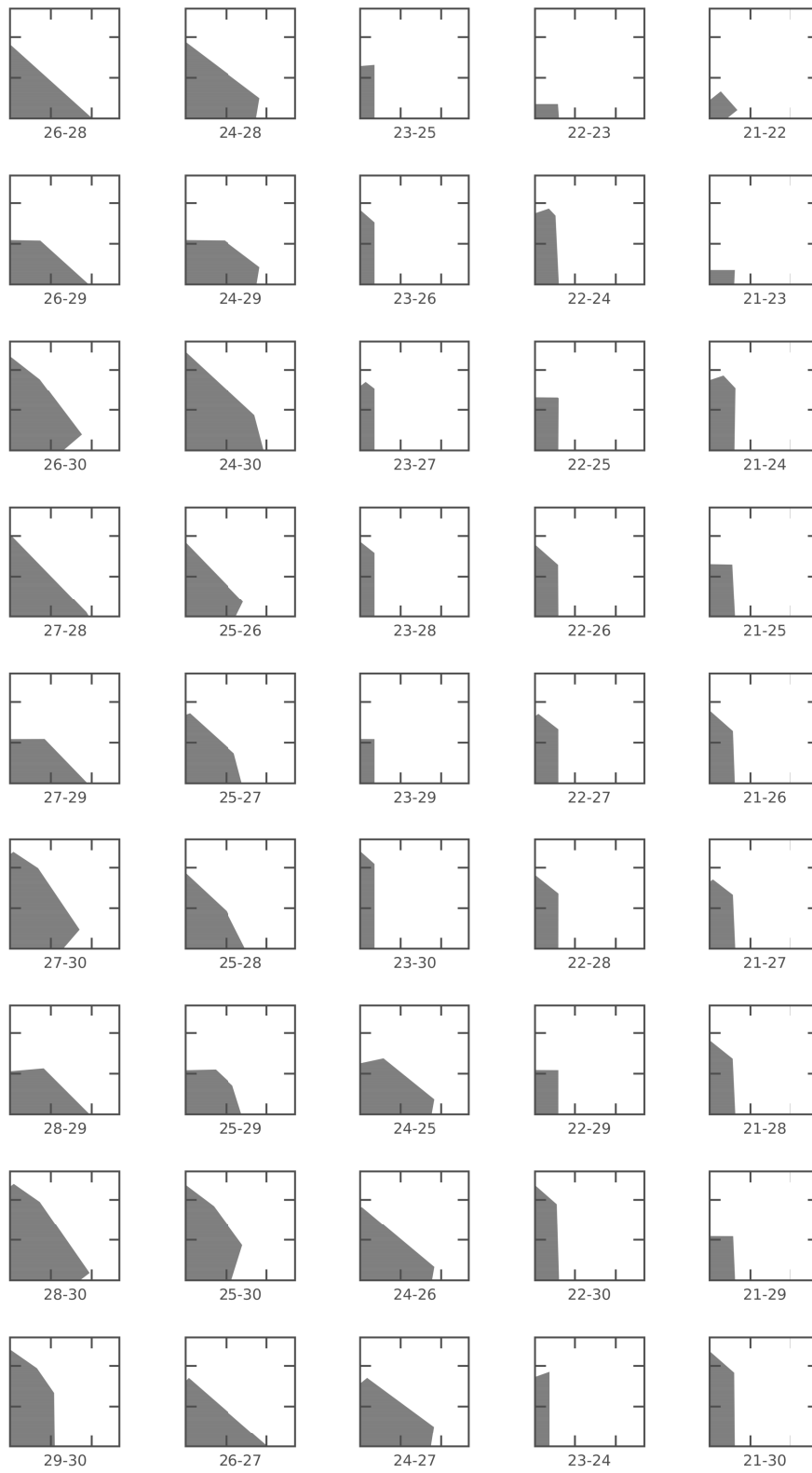












Bibliography

- [1] World's largest machine—the electric grid—is old and outdated. *Scientific American*. [Accessed 28.11.2017].
- [2] Bundesnetzagentur. Bericht der Bundesnetzagentur für Elektrizität, Gas, Telekommunikation, Post und Eisenbahnen über die Systemstörung im deutschen und europäischen Verbundsystem am 4. November 2006, 2007.
- [3] J. Machowski, J. Bialek, and J. Bumby. *Power System Dynamics: Stability and Control*. Wiley, 2011.
- [4] UCTE Operation Handbook, 2004. Available at <https://www.entsoe.eu>.
- [5] M. Anvari, G. Lohmann, M. Wächter, P. Milan, E. Lorenz, D. Heinemann, R. M. Rahimi Tabar, and J. Peinke. Short term fluctuations of wind and solar power systems. *New J. Phys.*, 18:063027, 2016.
- [6] P. Milan, M. Wächter, and J. Peinke. Stochastic modeling and performance monitoring of wind farm power production. *J. Ren. Sust. En.*, 6:033119, 2014.
- [7] Deutscher Industrie- und Handelskammertag. ECOPOST Neues rund um Umwelt, Energie, Klima und Rohstoffe.
- [8] S. Backhaus and M. Chertkov. Getting a grip on the electrical grid. *Phys. Today*, 66:42–48, 2013.
- [9] M. Timme, L. Kocarev, and D. Witthaut. Focus on networks, energy and the economy. *New J. Phys.*, 17:110201, 2015.
- [10] S. Auer, J. Heitzig, U. Kornek, and J. Kurths. The dynamics of coalition formation on complex networks. *Sci. Rep.*, 5:13366, 2015.
- [11] M. Mureddu, G. Caldarelli, A. Damiano, and H. Meyer-Ortmanns. Islanding the power grid on the transmission level: less connections for more security. *Phys. Rep.*, 6:34797, 2016.
- [12] H. Kim, S.H. Lee, and P. Holme. Building blocks of the basin stability of power grids. *Phys. Rev. E*, 93:062318, 2016.
- [13] D. Witthaut, M. Rohden, X. Zhang, S. Hallerberg, and M. Timme. Critical links and nonlocal rerouting in complex supply networks. *Phys. Rev. Lett.*, 116:138701, 2016.
- [14] P.J. Menck, J. Heitzig, J. Kurths, and H.J. Schellnhuber. How dead ends undermine power grid stability. *Nat. Comm.*, 5:3969, 2014.
- [15] K. Schmietendorf, J. Peinke, R. Friedrich, and O. Kamps. Self-organized synchronization and voltage stability in networks of synchronous machines. *Eur. Phys. J. Spec. Top.*, 223:2577–2592, 2014.

- [16] D. Witthaut and M. Timme. Nonlocal failures in complex supply networks by single link additions. *Eur. Phys. J. B*, 86(9):377, 2013.
- [17] D. Jung and S. Kettemann. Long-range response in ac electricity grids. *Phys. Rev. E*, 94:012307, 2016.
- [18] S.V. Buldyrev, R. Parshani, G. Paul, H.E. Stanley, and S. Havlin. Catastrophic cascade of failures in interdependent networks. *Nature*, 464:1025–1028, 2010.
- [19] J. Shao, S.V. Buldyrev, S. Havlin, and H.E. Stanley. Cascade of failures in coupled network systems with multiple support-dependence relations. *Phys. Rev. E*, 83:036116, 2011.
- [20] M. Rohden, D. Witthaut, M. Timme, and H. Meyer-Ortmanns. Curing critical links in oscillator networks as power flow models. *New J. Phys.*, 19:013002, 2017.
- [21] V. Frolov, S. Backhaus, and M. Chertkov. Efficient algorithm for locating and sizing series compensation devices in large power transmission grids: I. Model implementation. *New J. Phys.*, 16:105015, 2014.
- [22] K.S. Reddy, Madhusudan Kumar, T.K. Mallick, H. Sharon, and S. Lokeswaran. A review of integration, control, communication and metering (ICCM) of renewable energy based smart grid. *Renewable and Sustainable Energy Reviews*, 38:180 – 192, 2014.
- [23] M. Chertkov, M.G. Stepanov, F. Pan, and R. Baldick. Exact and efficient algorithm to discover extreme stochastic events in wind generation over transmission power grids. In *Proceedings of the 50th IEEE Conference on Decision and Control and European Control Conference, CDC-ECC 2011 - Orlando, FL, United States*, pages 2174–2180, 2011.
- [24] R.B. Hickey. *Electrical Engineer’s Portable Handbook*. Portable Handbook. McGraw-Hill Education, 2003.
- [25] R. Flosdorff and G. Hilgarth. *Elektrische Energieverteilung*. Leitfaden der Elektrotechnik. Vieweg+Teubner Verlag, 2005.
- [26] B. R. Oswald. Verlust- und Verlustenergieabschätzung. <http://www.netzausbau-niedersachsen.de/downloads/verlustvergleichwahlemecklarfinalv2.pdf>, 2007. [Accessed 28.11.2017].
- [27] Bundesnetzagentur. Monitoringbericht 2014, 2014. [Accessed 28.11.2017].
- [28] DeutscheUmwelthilfe. Aufbau des Stromnetzes. http://www.forum-netzintegration.de/uploads/media/DUH_Kurzinfo_Stromnetzaufbau.pdf. [Accessed 28.11.2017].
- [29] 50Hertz Transmission GmbH, Amprion GmbH, TenneT TSO GmbH and TransnetBW GmbH. Netzentwicklungsplan Strom. <https://www.netzentwicklungsplan.de/de>. [Accessed 29.11.2017].
- [30] ENTSO-E Transparency Platform. <https://transparency.entsoe.eu/>. [Accessed 17.01.2018].
- [31] STROM REPORT: Statistiken und Infografiken aus den Bereichen Energie und Umwelt. <https://1-stromvergleich.com/strom-report>. [Accessed 29.11.2017].

- [32] Carsten Matke, Wided Medjroubi, and David Kleinhans. SciGRID - An Open Source Reference Model for the European Transmission Network (v0.2), July 2016.
- [33] A. von Meier. *Electric Power Systems: A Conceptual Introduction*. Wiley Survival Guides in Engineering and Science. Wiley, 2006.
- [34] Ray D. Zimmerman and Carlos E. Murillo-Sánchez. Matpower 6.0 User’s Manual. <http://www.pserc.cornell.edu/matpower/>. [Accessed 28.11.2017].
- [35] W. Mathis, K. Küpfmüller, A. Reibiger, and G. Kohn. *Theoretische Elektrotechnik und Elektronik: Eine Einführung*. Springer-Lehrbuch. Springer Berlin Heidelberg, 2013.
- [36] Bureau International des Poids et Mesures. The International System of Units (SI). 2006.
- [37] Electronicstutorials. <http://www.electronics-tutorials.ws/>. [Accessed 20.12.2017].
- [38] Jim McCalley and Leigh Tesfatsion. The power flow equations. http://home.eng.iastate.edu/~jdm/ee458_2011/PowerFlowEquations.pdf, 2011. [Accessed 28.11.2017].
- [39] Power Systems Analysis Software. https://wiki.openelectrical.org/index.php?title=Power_Systems_Analysis_Software. [Accessed 05.12.2017].
- [40] Ray Daniel Zimmerman, Carlos Edmundo Murillo-Sánchez, and Robert John Thomas. Matpower: Steady-state operations, planning, and analysis tools for power systems research and education. *IEEE Transactions on power systems*, 26(1):12–19, 2011.
- [41] T. Brown, J. Hörsch, and D. Schlachtberger. PyPSA: Python for Power System Analysis. *Journal of Open Research Software*, 6(4), 2018.
- [42] Open Power System Data- A free open data platform for power system modelling. <https://open-power-system-data.org/>. [Accessed 29.11.2017].
- [43] open_eGo - Open Electricity Grid Optimization. <https://openegoproject.wordpress.com/>. [Accessed 29.11.2017].
- [44] G.N. Tiwari and R.K. Mishra. *Advanced Renewable Energy Sources*. Royal Society of Chemistry, 2015.
- [45] F. Raischel, T. Scholz, V.V. Lopes, and Pedro G. Lind. Uncovering wind turbine properties through two-dimensional stochastic modeling of wind dynamics. *Phys. Rev. E*, 88:042146, 2013.
- [46] G Bel, C P Connaughton, M Toots, and M M Bandi. Grid-scale fluctuations and forecast error in wind power. *New J. Phys.*, 18(2):023015, 2016.
- [47] James R. Salmona and John L. Walmsleyb. A two-site correlation model for wind speed, direction and energy estimates. *J. Wind Eng. & Indust. Aerodyn.*, 79(3):233–268, 1999.
- [48] Anna R. Mehrens, Andrea N. Hahmann, Xiaoli G. Larsen, and Lueder von Bremen. Correlation and coherence of mesoscale wind speeds over the sea. *Quart. J. Roy. Meteo. Soc.*, 142(701):3186–3194, 2016.

-
- [49] FINO1 - Forschungsplattformen in Nord- und Ostsee Nr. 1. <http://www.fino1.de/en/>. [Accessed 29.11.2017].
- [50] S. Tuller and A. Brett. The characteristics of wind velocity that favor the fitting of a weibull distribution in wind speed analysis. *J. Appl. Meteorol.*, 23:124–134, 1984.
- [51] C. Carrillo, J. Cidrás, E. Díaz-Dorado, and A. F. Obando-Montaño. An approach to determine the weibull parameters for wind energy analysis: the case of galicia (spain). *Energies*, 7:2676–2700, 2014.
- [52] M. Abramowitz and I.A. Stegun. *Handbook of Mathematical Functions*. NBS National Bureau of Standards, 1972.
- [53] Inc. The MathWorks. *MATLAB and Optimization Toolbox Release 2016b*. 2016.
- [54] Christoph Schiel, Pedro G Lind, and Philipp Maass. Resilience of electricity grids against transmission line overloads under wind power injection at different nodes. *Scientific Reports*, 7(1):11562, 2017.
- [55] C. Grigg, P. Wong, P. Albrecht, R. Allan, M. Bhavaraju, R. Billinton, Q. Chen, C. Fong, S. Haddad, S. Kuruganty, and et al. The IEEE Reliability Test System 1996. A report prepared by the reliability test system task force of the application of probability methods subcommittee. *IEEE Trans. Pow. Sys.*, 14:1010–1020, 1999.
- [56] MATLAB. *version R2017a*. The MathWorks Inc., Natick, Massachusetts, 2017.
- [57] QGIS Development Team. QGIS Geographic Information System. Open Source Geospatial Foundation Project. <http://qgis.osgeo.org>", 2017. [Accessed 28.11.2017].
- [58] Emden R. Gansner and Stephen C. North. An open graph visualization system and its applications to software engineering. *SOFTWARE - PRACTICE AND EXPERIENCE*, 30(11):1203–1233, 2000.

Erklärung über die Eigenständigkeit der erbrachten wissenschaftlichen Leistung

Ich erkläre hiermit, daß ich die vorliegende Arbeit ohne unzulässige Hilfe Dritter und ohne Benutzung anderer als der angegebenen Hilfsmittel angefertigt habe. Die aus anderen Quellen direkt oder indirekt übernommenen Daten und Konzepte sind unter Angaben der Quelle gekennzeichnet.

Bei der Auswahl und Auswertung folgenden Materials haben mir die nachstehend aufgeführten Personen in der jeweils beschriebenen Weise entgeltlich/unentgeltlich geholfen:

1. _____

2. _____

3. _____

Weitere Personen waren an der inhaltlichen materiellen Erstellung der vorliegenden Arbeit nicht beteiligt. Insbesondere habe ich hierfür nicht die entgeltliche Hilfe von Vermittlungs- bzw. Beratungsdiensten (Promotionsberater oder andere Personen) in Anspruch genommen. Niemand hat von mir unmittelbar oder mittelbar geldwerte Leistungen für Arbeiten erhalten, die im Zusammenhang mit dem Inhalt der vorgelegten Dissertation stehen.

Die Arbeit wurde bisher weder im In- noch im Ausland in gleicher oder ähnlicher Form einer anderen Prüfungsbehörde vorgelegt.

Ort, Datum

Unterschrift